Ameliorating the Courant-Friedrichs-Lewy condition in spherical coordinates: A double FFT filter method for general relativistic MHD in dynamical spacetimes

Liwei Ji,[1,*] Vassilios Mewes,[2] Yosef Zlochower,[1] Lorenzo Ennoggi,[1] Federico G. Lopez Armengol,[3,1]
Manuela Campanelli,[1] Federico Cipolletta,[4] and Zachariah B. Etienne[5,6,7]

[1]*Center for Computational Relativity and Gravitation, and School of Mathematical Sciences,
Rochester Institute of Technology, 85 Lomb Memorial Drive, Rochester, New York 14623, USA*
[2]*National Center for Computational Sciences, Oak Ridge National Laboratory,
P.O. Box 2008, Oak Ridge, Tennessee 37831-6164, USA*
[3]*NPCx, 23150 Fashion Drive, Suite 238 Estero, Florida 33928, USA*
[4]*Barcelona Supercomputing Center (BSC), Plaça d'Eusebi Güell, 1-3, 08034 Barcelona, Spain*
[5]*Department of Physics, University of Idaho, Moscow, Idaho 83843, USA*
[6]*Department of Physics and Astronomy, West Virginia University,
Morgantown, West Virginia 26506, USA*
[7]*Center for Gravitational Waves and Cosmology, West Virginia University,
Chestnut Ridge Research Building, Morgantown, West Virginia 26505, USA*

Numerical simulations of merging compact objects and their remnants form the theoretical foundation for gravitational wave and multimessenger astronomy. While Cartesian-coordinate-based adaptive mesh refinement is commonly used for simulations, spherical-like coordinates are more suitable for nearly spherical remnants and azimuthal flows due to lower numerical dissipation in the evolution of fluid angular momentum, as well as requiring fewer numbers of computational cells. However, the use of spherical coordinates to numerically solve hyperbolic partial differential equations can result in severe Courant-Friedrichs-Lewy (CFL) stability condition time step limitations, which can make simulations prohibitively expensive. This paper addresses this issue for the numerical solution of coupled spacetime and general relativistic magnetohydrodynamics evolutions by introducing a double fast Fourier transform (FFT) filter and implementing it within the fully message passing interface (MPI)-parallelized SphericalNR framework in the Einstein Toolkit. We demonstrate the effectiveness and robustness of the filtering algorithm by applying it to a number of challenging code tests, and show that it passes these tests effectively, demonstrating convergence while also increasing the time step significantly compared to unfiltered simulations.

I. INTRODUCTION

With the advent of gravitational wave and multimessenger astronomy [1–9], there is an ever greater need for high-accuracy, long-term numerical simulations of merging compact objects and their remnants, such as the first general relativistic hydrodynamics (GRHD) binary neutron star (NS) merger simulation [10], the first simulations of binary black hole (BH) mergers [11–13], the first GRHD BH-NS merger simulation [14], the first general relativistic magnetohydrodynamics (GRMHD) BNS merger simulations [15,16], and the first GRMHD simulation of BH-NS mergers [17]. See the review articles [18–26] and references therein for recent advances in the field. Traditionally, such simulations are performed using Cartesian coordinates, which leads to simpler numerical algorithms and very robust codes. However, such coordinates are also computationally wasteful, as they over-resolve in the angular directions leading to the necessity of mesh refinement in order to prevent computationally prohibitive cell counts in large computational domains.

An alternative approach is to use coordinates adapted to the symmetries (approximate or exact) associated with the numerical problem. In particular, the nearly spherical remnant associated with a compact-object merger is ideally suited for spherical-like coordinates due to the lower numerical dissipation in the evolution of fluid angular momentum compared to Cartesian coordinates [27]. Another area are GRMHD simulations of accretion disks, where it is customary to use spherical-like coordinates (see, for instance, the Einstein Horizon Telescope code comparison project [28]). With this in mind, we recently

*ljsma@rit.edu

104005-1

introduced SphericalNR [29], a fully MPI-parallelized implementation of the Baumgarte-Shapiro-Shibata-Nakamura (BSSN) [30,31] formulation of the Einstein equations in spherical coordinates within the Einstein Toolkit [32,33]. The code was later extended to include GRMHD [34] in the reference metric formalism [35] and constraint damping in the spacetime evolution via the fully covariant and conformal formulation of the Z4 system, fCCZ4 [34,36–38].

The attractive features of using spherical coordinates for the simulation of azimuthal flows comes with a price; however, as the use of spherical coordinates can lead to a severe Courant-Friedrichs-Lewy stability condition (CFL) [39] limitation of the allowable time step associated with the polar axis and origin of the spherical coordinate system when solving hyperbolic partial differential equations. This is due to the cell volumes (and therefore time steps) becoming prohibitively small as the polar axis and origin are approached. Compared to Cartesian coordinates, where the time step is $\propto dx_{\min}$, in spherical coordinates the time step is $\propto r\sin\theta d\varphi$, which can render high resolution, long-term numerical simulations in 3D prohibitively expensive. There are various approaches to remedy the problem, including multiblock or multipatch techniques [40–57], tessellated grids [58,59], static mesh refinement [60–62], mesh coarsening [63–66], local filters [67–69], global FFT filters [63], and distorted angular grids [70,71], to name a few. Each approach to solve the CFL limitation has its own advantages and limitations, such as algorithmic complexity, ensuring conservation, or the use of global operations.

In SphericalNR, we have chosen to implement a double FFT filter that filters spacetime and GRMHD fields in both the θ and φ directions depending on radius and latitude (for the filtering in φ). FFT filtering has both conceptual and algorithmic difficulties: In general, the evolved GRMHD fields can develop discontinuities, which requires a different filter algorithm than filtering smooth fields by exponentially damping CFL unstable modes. Further, the FFT filter is a global operation of either an entire great circle when filtering in θ or an entire φ coordinate ring. An earlier version of the FFT filter that was only OPENMP-parallelized and filtering in the φ coordinate only was used in [34,72]. This severely limited the applicability of the filter to high-resolution simulations due to the inability to decompose the domain in φ. In this work, we have extended the FFT filter to work in both angular coordinates and have fully MPI-parallelized it. We have developed an automatic switch to filter the GRMHD fields with a Gaussian filter instead of an exponential filter, which prevents spurious oscillations as a result of filtering discontinuous fields.

This paper is organized as follows. In Sec. II, we describe the techniques we use to both evolve the BSSN/fCCZ4 system coupled to GRMHD and how we filter the unstable polar and azimuthal modes in the double FFT filter, as well as describing the details of the filter parallelization.

In Sec. III, we show the results of applying our filtering algorithm to a single spinning Bowen-York black hole (BH), an off-center spherical explosion, an off-center stable rotating neutron star (NS), and a rotating NS that is susceptible to the dynamical bar-mode instability. Finally, in Sec. IV, we discuss our results. We use the Einstein summation convention throughout. Unless otherwise stated, all results are presented in units in which $G = M_\odot = c = 1$.

II. TECHNIQUES

In previous papers, our collaboration described a fully parallelized implementation of the vacuum Einstein equations and GRMHD using spherical coordinates [29,34] within the Einstein Toolkit. Here, we describe a series of modifications that allow us to use that code without the sometimes severe CFL limitation on the time step. Our code is based on the fCCZ4 formalism of Einstein equations and the *Valencia* formulation of GRMHD [73,74] and uses the Einstein Toolkit to provide parallelization and critical analysis tools. The Einstein Toolkit is an open-source code suite for relativistic astrophysics simulations. It uses the modular CACTUS [75] framework [76] (consisting of general modules called "thorns") and provides adaptive box-in-box mesh refinement (AMR) via the CARPET [77] code [78].

In the present work, we introduce two main modifications to the standard evolution techniques described in [29,34], these are the introduction of a double FFT filtering scheme to ameliorate the severe CFL limitations associated with spherical coordinates and a generic fisheye [79] radial coordinate to more efficiently allocate the grid points (we also introduce modifications to the standard shift conditions that appears to perform better in some of our tests). While we do choose a few particular "fisheye" coordinates here, for example,

$$r = Ax_1 + (1 - A)r_0\mathrm{atan}(x_1/r_0), \qquad (1)$$

where r is the usual radial coordinate, x_1 is the "fisheye" radial coordinate (the actual numerical coordinate), the constant A determines the ratio of the physical to numerical gird spacing far from the origin (by construction, this ratio is 1 at the origin), and r_0 is a parameter to fine-tune where the transition occurs, the code can work with any one-to-one differentiable function $r(x_1)$. In particular, we performed several simulations with an *exponential* "fisheye", $r(x_1) \propto \exp(x_1)$, commonly used in GRMHD simulations of accretion disks (see, e.g., some of the codes used in [28]).

We give a summary of the evolution system below and refer the reader to the full details in [34,80–82]. Central to the method is the conformally related spatial metric,

$$\bar{\gamma}_{ij} = e^{-4\phi}\gamma_{ij}, \qquad (2)$$

where γ_{ij} is the physical spatial metric, and ϕ the conformal factor,

$$e^{4\phi} = (\gamma/\bar{\gamma})^{1/3}, \tag{3}$$

where γ and $\bar{\gamma}$ are the determinants of the physical and conformally related metric, respectively. In order to make the conformal rescaling unique, we adopt Brown's "Lagrangian" choice [83],

$$\partial_t \bar{\gamma} = 0, \tag{4}$$

fixing $\bar{\gamma}$ to its initial value throughout the evolution. Similarly, the conformally related extrinsic curvature is defined as

$$\bar{A}_{ij} = e^{-4\phi}\left(K_{ij} - \frac{1}{3}\gamma_{ij}K\right), \tag{5}$$

where K_{ij} is the physical extrinsic curvature and $K = \gamma^{ij}K_{ij}$ its trace.

The main idea is to write the conformally related metric as the sum of the flat background metric plus perturbations (which need not be small),

$$\bar{\gamma}_{ij} = \hat{\gamma}_{ij} + \epsilon_{ij}, \tag{6}$$

where $\hat{\gamma}_{ij}$ is the reference metric in fisheye spherical coordinates,

$$\hat{\gamma}_{ij} = \begin{pmatrix} \left(\frac{dr(x_1)}{dx_1}\right)^2 & 0 & 0 \\ 0 & r(x_1)^2 & 0 \\ 0 & 0 & r(x_1)^2 \sin^2\theta \end{pmatrix}. \tag{7}$$

The conformal connection coefficients $\bar{\Lambda}^i$ are treated as independently evolved variables that satisfy the initial constraint,

$$\bar{\Lambda}^i - \Delta^i = 0. \tag{8}$$

Here,

$$\Delta^i \equiv \bar{\gamma}^{jk}\Delta^i_{jk}, \tag{9}$$

and Δ^i_{jk} is the difference between the Christoffel symbols of the conformally rescaled and flat reference metric,

$$\Delta^i_{jk} \equiv \bar{\Gamma}^i_{jk} - \hat{\Gamma}^i_{jk}. \tag{10}$$

The conformal connection coefficients $\bar{\Lambda}^i$, therefore, transform like vectors in the reference-metric formalism. Together with the lapse α and the shift β^i, this set of the $3+1$ variables $\{\alpha, \beta^i, \gamma_{ij}, K_{ij}\}$, expressed in spherical

coordinates, is stored in the thorn ADMBASE to interface with existing diagnostics in the Einstein Toolkit.

When evolving the fCCZ4 (and other systems similar to BSSN) equations, we use the $1+\log$ slicing conditions [84],

$$\partial_t \alpha = \beta^i \partial_i \alpha - 2\alpha K, \tag{11}$$

and shift conditions [83,85],

$$\partial_t B^i = \frac{3}{4}\partial_t \bar{\Lambda}^i - \kappa_B \frac{3}{4}\beta^j \hat{D}_j \bar{\Lambda}^i - \eta B^i,$$
$$\partial_t \beta^i = B^i, \tag{12}$$

where $\hat{D}_i$ is the covariant derivative with respect to the background flat metric and $\kappa_B = 0$ leads to the standard nonadvected Γ-driver shift, while $\kappa_B = 1$ leads to a modification that proved to be more accurate for spacetimes containing BH.

A key idea for regularizing the fCCZ4 (and other) systems in spherical coordinates is to evolve tensorial quantities in a basis that is orthonormal with respect to the background conformal metric. To distinguish between coordinate-basis components and orthonormal-basis components, we will follow the notation of [34]. Suppose $T^{i_1 i_2 \cdots}{}_{j_1 j_2 \cdots}$ are the coordinate components of a tensor T, then the orthonormal components will be denoted by $T^{\{a_1\}\{a_2\}\cdots}{}_{\{b_1\}\{b_2\}\cdots}$, where

$$T^{\{a_1\}\{a_2\}\cdots}{}_{\{b_1\}\{b_2\}\cdots}$$
$$= \mathbf{e}^{\{a_1\}}_{i_1}\mathbf{e}^{\{a_2\}}_{i_2}\cdots\mathbf{e}^{j_1}_{\{b_1\}}\mathbf{e}^{j_2}_{\{b_2\}}\cdots T^{i_1 i_2 \cdots}{}_{j_1 j_2 \cdots}, \tag{13}$$

and $\mathbf{e}^{\{j\}}_i$ and $\mathbf{e}^i_{\{j\}}$ are elements of the (background) orthonormal vector and covector bases, respectively. In our notation, $\mathbf{e}^{\{i\}}_j$ represents the jth coordinate component of the ith basis element.

The background orthonormal vector basis takes the form,

$$\mathbf{e}^j_{\{r\}} = \left(\frac{1}{r'(x_1)}, 0, 0\right), \tag{14}$$

$$\mathbf{e}^j_{\{\theta\}} = \left(0, \frac{1}{r(x_1)}, 0\right), \tag{15}$$

$$\mathbf{e}^j_{\{\varphi\}} = \left(0, 0, \frac{1}{r(x_1)\sin\theta}\right), \tag{16}$$

with the corresponding orthonormal cobasis,

$$\mathbf{e}^{\{r\}}_j = (r'(x_1), 0, 0), \tag{17}$$

$$\mathbf{e}_j^{\{\theta\}} = (0, r(x_1), 0), \qquad (18)$$

$$\mathbf{e}_j^{\{\varphi\}} = (0, 0, r(x_1) \sin\theta). \qquad (19)$$

In this system, our evolution variables are $\epsilon_{\{i\}\{j\}}$, $A_{\{i\}\{j\}}$, etc. To convert the coordinate-component evolution equation to the orthonormal-basis components, we express derivative of the coordinate-component tensors in terms of analytical derivatives of the basis and finite-difference derivatives of the tensor components. For example, an expression like

$$\partial_i A_{jk} \qquad (20)$$

becomes

$$\partial_i \left(\mathbf{e}_j^{\{l\}} \mathbf{e}_k^{\{m\}} A_{\{l\}\{m\}} \right)$$
$$= \partial_i \left(\mathbf{e}_j^{\{l\}} \mathbf{e}_k^{\{m\}} \right) A_{\{l\}\{m\}} + \mathbf{e}_j^{\{l\}} \mathbf{e}_k^{\{m\}} \partial_i A_{\{l\}\{m\}}, \qquad (21)$$

where $\partial_i A_{\{l\}\{m\}}$ is evaluated using finite differences and the derivatives of the basis elements are calculated analytically.

The numerical code for the right-hand side in the fCCZ4 evolution system as well as GRMHD source terms are provided by the SENR/NRPY+ code, and the time integration is performed with the method of lines as implemented in the MOL [33] thorn. We have implemented a fourth-order strong stability-preserving Runge-Kutta (SSPRK54) method [86] in MOL, which has larger CFL factor than the more traditional RK2 or RK3 [87,88] methods and is large enough to compensate for the extra computational work due to SSRK54 having more stages.

We refer the reader to [29,34,80–82] for the full details of the evolution system but note that, compared to [34], we have made several improvements to the GRMHD code in SphericalNR: We have developed a custom built ninth order WENO-Z9 reconstruction (local smoothness indicators β_k written as perfect squares [89], optimal higher order global smoothness indicators τ_{r2-1} [90], and adaptive ϵ [91]). There is also the option to combine the WENO-Z9 reconstruction with the monotonicity-preserving (MP) limiter [92], resulting in a MPWENO scheme [93]. We have implemented the consistency-ensuring summation of [94], which when applied to the MP limiting algorithm helps alleviating the spontaneous symmetry breaking and associated drifts we observed in [34] when using MP5 reconstruction. We have also implemented seventh and ninth order MP7 and MP9 [92], but find that, even using consistency-ensuring summation, MPWENO-Z9 is still more robust in that regard (and WENO-Z9 better still). When using higher order reconstruction methods, the reconstructed density or pressure might occasionally become negative; in which case, we reconstruct them using a total variation diminishing (TVD) reconstruction with the

minmod limiter. We have also implemented higher order flux corrections of [95] using cell-centered fluxes as higher order corrections to face fluxes as in [96]. The WENO-Z9 method will be described in detail in a forthcoming paper regarding the use of higher order methods in GRMHD simulations of BH accretion flows.

When using WENO-Z9 in simulations (we can still use any of the existing reconstruction methods available in the original GRHydro code [97]), we typically evolve the magnetic vector potential A_i and the electromagnetic scalar potential $\hat{\Phi}$ using tenth order central finite differences and use ninth order Kreiss-Oliger (KO) dissipation [98] to damp high frequency noise in the evolution of A_i and $\hat{\Phi}$. We obtain the magnetic field B^i from A_i using tenth order finite differences when calculating the curl of A_i. Accordingly, we use tenth ordered central finite differences in the source terms [Eqs. (73) and (80) in [34]]. Unless otherwise noted in Sec. III below, we have used WENO-Z9 and tenth order central finite differences.

We note that these higher-order methods do require more ghost zones, which can have an impact on speed. A tenth-order central stencil requires five ghost zones.

Finally, in order to improve the robustness of the GRMHD evolution, we have also made several improvements, in particular to the primitive variable recovery and artificial atmosphere. Before attempting primitive recovery, we enforce the following condition on the conserved variables found in Appendix C of [99]:

$$\tau = \max \left(\tau, \sqrt{\gamma} \left((\rho\epsilon)_{\text{floor}} + \frac{B^2}{2} \right) \right), \qquad (22)$$

as well as steps (2) and (3) of said Appendix. We then use the primitive variable recovery scheme of [100]. If the initial recovery fails, we try again using the initial guesses of [101]. In the regions where the primitive variable recovery becomes increasingly difficult (low plasma-$\beta 2P/b^2$, high internal energy density ϵ, high Lorentz factor W), the primitive recovery is still prone to fail. To alleviate this problem, we follow [102,103] and evolve the conserved entropy in the reference metric formalism,

$$\partial_t \mathcal{S} + \hat{\mathcal{D}}_i \left(\alpha \mathcal{S} \left(v^i - \frac{\beta^i}{\alpha} \right) \right) = 0, \qquad (23)$$

where

$$\mathcal{S} = e^{6\phi} \sqrt{\frac{\bar{\gamma}}{\hat{\gamma}}} W \frac{P}{\rho^{\Gamma-1}}, \qquad (24)$$

and $\hat{\mathcal{D}}$ is the covariant derivative associated with the spherical background metric $\hat{\gamma}_{ij}$, α the lapse, v^i the Valencia fluid three-velocity, β^i the shift, ϕ the conformal factor, $\bar{\gamma}$ the determinant of the conformal metric $\bar{\gamma}_{ij}$, $\hat{\gamma}$ the

determinant of the spherical background metric, P the fluid pressure, ρ the fluid rest-mass density, and Γ the adiabatic index, respectively (see [34] for details on the evolution equations in the reference metric formalism). We always use a TVD reconstruction with the minmod limiter for the reconstruction of the entropy. After each successful primitive recovery, $\mathcal{S}$ is recalculated from the primitives and evolved for a Runge-Kutta substep. We recover the pressure P from $\mathcal{S}$ wherever $\beta^{-1} = b^2/(2P) > 100$ or using the recovery scheme of [100] failed. While this approach guarantees a positive pressure, the recovery can still fail, in which case, we follow [103] and try to average the primitives from neighboring cells that had a successful recovery; otherwise, the primitives are set to atmosphere values with $v^i = 0$. The magnetic field B^i is never touched and always calculated from the curl of A_i.

For the artificial atmosphere, we have implemented both isotropic and radially dependent floors for the density and pressure, where

$$\rho_{\text{floor}} = \rho_{\text{atmo}} \max(r_{\text{min}}, r)^{-1.5} \tag{25}$$

$$\begin{aligned} P_{\text{floor}} &= (\Gamma - 1)(\rho\epsilon)_{\text{floor}} \\ &= (\Gamma - 1)(\rho\epsilon)_{\text{atmo}} \max(r_{\text{min}}, r)^{-1.5\Gamma}, \end{aligned} \tag{26}$$

where r_{min} is a parameter to avoid the floors from diverging at the origin. Where evolved cells fall below these floor values, we just raise ρ or P to their floor values, and if $10b^2 > \min(\rho, p/(\Gamma - 1))$, we add matter in the drift frame [104] instead. When using the approximate HLLE (Harten-Lax-van Leer-Einfeldt) Riemann solver [105,106], we switch to the more diffusive global (with a characteristic speed of 1) Lax-Friedrichs fluxes wherever the magnetization $\sigma = \frac{b^2}{\rho} > 1$, the inverse plasma $\beta^{-1} > 100$, $\rho < 10\rho_{\text{floor}}$, $\rho\epsilon < 10(\rho\epsilon)_{\text{floor}}$, or a grid point is inside an apparent horizon. The entropy equation (23) is always evolved with the Lax-Friedrichs flux and a global characteristic speed of 1. We also impose a ceiling (typically 50) on W, and a ceiling on ϵ. After these potential fixes to the primitive variables are done, we recompute the conserved variables everywhere. While this breaks strict conservation, it is necessary to maintain a consistent set of conserved and primitive variables.

Finally, inspired by other GRMHD codes [61,107], at the $r = 0$ cell faces, we set the reconstructed electric field components $E_\theta = E_\varphi = 0$, and for the $\theta = 0, \pi$ cell faces, set $E_r = E_\varphi = 0$.

A. Filtering algorithms

We use the FFTW3 [108] library to perform all Fourier transforms. The main idea of the algorithm is to dampen CFL unstable modes at a given radius and latitude by performing FFTs in both polar and azimuthal directions, modifying the Fourier expansion of the evolved fields, and

then performing the inverse FFT to obtain the filtered fields in real space. The double FFT filter first performs FFT filtering in the θ direction followed by FFT filtering in the φ direction. In order to be able to filter in the θ direction, we define a new angular coordinate, ϑ, which extends the θ coordinate from $[0, \pi]$ to $[0, 2\pi]$. To do this, we first construct the field $\mathbf{X}(x_1, \vartheta, \varphi)$,

$$\mathbf{X}(x_1, \vartheta, \varphi) = \begin{cases} \mathbf{X}(x_1, \theta, \varphi), & \vartheta \in [0, \pi] \\ (-1)^a \mathbf{X}(x_1, \pi - \theta, \pi + \varphi), & \vartheta \in [\pi, 2\pi] \end{cases}, \tag{27}$$

where $a = 0$ or 1, depending on the axis parity factor of the field, i.e., positive or negative parity, respectively (see Table I in [34]). We then perform a FFT in the ϑ coordinate on $\mathbf{X}(x_1, \vartheta, \varphi)$ to obtain the Fourier expansion $\tilde{\mathbf{X}}(x_1, l, \varphi)$ (note that l denotes Fourier mode in the θ direction), which is then filtered and finally obtain the filtered field $\mathbf{X}(x_1, \vartheta, \varphi)$ by performing the inverse FFT,

$$\mathbf{X}(x_1, \vartheta, \varphi) \xrightarrow{\text{FFT}} \tilde{\mathbf{X}}(x_1, l, \varphi) \to f(l, l_{\text{max}}) \tilde{\mathbf{X}}(x_1, l, \varphi) \\ \xrightarrow{\text{iFFT}} \mathbf{X}(x_1, \vartheta, \varphi), \tag{28}$$

where the filtering function $f(l, l_{\text{max}})$ depends on the type of field being filtered and will be described below [see (39) and (40)]. We then filter the evolved fields in the φ direction analogously,

$$\mathbf{X}(x_1, \theta, \varphi) \xrightarrow{\text{FFT}} \tilde{\mathbf{X}}(x_1, \theta, m) \to f(m, m_{\text{max}}) \tilde{\mathbf{X}}(x_1, \theta, m) \\ \xrightarrow{\text{iFFT}} \mathbf{X}(x_1, \theta, \varphi), \tag{29}$$

(note that m denotes Fourier modes in the φ direction). The maximum allowed modes l_{max} and m_{max} in the θ and φ filters are given by

$$l_{\text{max}} = \max\left(2, \frac{2r}{dr_{\text{min}}} \mathcal{L}\right), \tag{30}$$

$$m_{\text{max}} = \max\left(2, \frac{2r}{dr_{\text{min}}} \sin\theta \mathcal{L}\right), \tag{31}$$

where r is the physical coordinate radius (i.e., related to the compuational radial coordinate by a fisheye transformation) and dr_{min} is the smallest radial grid spacing on the computational domain. Because even along the pole and the origin the angular dependence of the evolved fields are nontrivial, we never filter out the first $\mathcal{L}$ modes (see discussion below).

If we would like to achieve a time step that is $\propto dr_{\text{min}}$, we would need to filter the evolved fields to m_{max} near the axis for even moderate angular resolutions. However, we can never (in, general) filter all the way to $m = 0$ and $l = 0$.

In the vicinity of both the poles and the origin, a regular metric in Cartesian coordinates will induce both $m = 1$ and $m = 2$ modes in the resulting spherical metric (in particular, the components in the orthonormal basis). This is easily shown by considering a generic metric in Cartesian coordinates in the vicinity of the pole (i.e., $x \sim 0$, $y \sim 0$, and $z = z_0$). The metric will, in general, be

$$ds^2 = (1 + a)dx^2 + 2bdxdy + 2cdxdz + (1 + d)dy^2$$
$$+ 2edydz + (1 + f)dz^2 + \mathcal{O}(x, y, z - z_0). \quad (32)$$

The resulting components of the metric in the background (spherical) orthonormal basis will contain terms proportional to $\exp(\pm i\varphi)$, $\exp(\pm i2\varphi)$, $\exp(\pm i\theta)$ and $\exp(\pm i2\theta)$. For example,

$$\gamma_{\{r\}\{r\}} = (a + 1)\sin^2(\theta)\cos^2(\varphi)$$
$$+ \sin(\varphi)(\sin^2(\theta)(2b\cos(\varphi) + (d + 1)\sin(\varphi))$$
$$+ e\sin(2\theta)) + c\sin(2\theta)\cos(\varphi)$$
$$+ (f + 1)\cos^2(\theta), \quad (33)$$

$$\gamma_{\{\varphi\}\{\varphi\}} = 1/2(2 + a + d + (-a + d)\cos[2\varphi]$$
$$- 2b\sin[2\varphi]), \quad (34)$$

$$\gamma_{\{\theta\}\{\varphi\}} = \cos(\theta)((d - a)\sin(\varphi)\cos(\varphi) + b\cos(2\varphi))$$
$$+ \sin(\theta)(c\sin(\varphi) - e\cos(\varphi)). \quad (35)$$

On the poles, these become

$$\gamma_{\{r\}\{r\}} = 1 + f, \quad (36)$$

$$\gamma_{\{\varphi\}\{\varphi\}} = 1 + ((d - a)\cos(2\varphi) + a - 2b\sin(2\varphi) + d)/2, \quad (37)$$

$$\gamma_{\{\theta\}\{\varphi\}} = (d - a)\sin(\varphi)\cos(\varphi) + b\cos(2\varphi). \quad (38)$$

Thus, at the origin, and on the poles, there should be $m = 2$ modes in both θ and φ (but no higher) if the metric in spherical coordinates is to reproduce this simple Cartesian metric.

To fully retain the $m = 2$ modes in both θ and φ, we could set all unwanted modes to zero (a spectrally sharp low-pass filter essentially) or use an exponential filter,

$$f_{\exp}(l, l_{\max}) = \begin{cases} 1, & |l| \le l_{\max} \\ e^{-(|l| - l_{\max})}, & l > l_{\max} \end{cases}, \quad (39)$$

which retains all power in modes $|l| \le l_{\max}$. We use the exponential filter for all evolved spacetime fields, which are smooth [109] and retaining full power in unfiltered modes therefore does not result in new extrema and potential Gibbs phenomenon during the filtering. This situation is

very different for the filtered GRMHD fields $(D, S_i, \tau, \mathcal{S}, A_i, \hat{\Phi})$, which can in general become discontinuous. Filtering discontinuous fields with the exponential filter would result in Gibbs phenomenon, leading to nonphysical oscillations and potentially nonpositive values (the latter will result in catastrophic failures that would need to be fixed in an posterior step after filtering, similar to what is done in the artificial atmosphere). To remedy this, we filter $(D, S_i, \tau, \mathcal{S})$ with a Gaussian filter,

$$f_{\text{Gaussian}}(l, l_{\max}) = \exp\left(\log(0.9)\left(\frac{l}{l_{\max} + 1}\right)^2\right), \quad (40)$$

while filtering the magnetic vector potential and electromagnetic scalar potential $(A_i, \hat{\Phi})$ with the exponential filter (39). The Gaussian filter avoids Gibbs phenomena at the expense of reducing the power in all Fourier modes apart from the $l, m = 0$ mode. While this guarantees that no new extrema are generated in the filtering process, the reduction in power in lower order modes negatively affects the overall resolution of the simulation. We have chosen a reduction in power to 0.9 in the first mode that is CFL unstable (i.e., the mode $l = l_{\max} + 1$) as a compromise between trying to reduce as little power as possible in the modes that are CFL stable (and should therefore not be filtered at all) while simultaneously guaranteeing the CFL unstable modes are sufficiently suppressed to prevent CFL instabilities in the evolution.

In our initial explorations of the tests presented in Sec. III, we found that maintaining full power in the modes up to $m = 2$ at the axis and origin are critical. We have therefore designed a hybrid filter that seeks to use the exponential filter wherever possible and switches to the Gaussian filter only when discontinuities are detected in the coordinate ring being filtered. For a field u, we try to detect discontinuities in the ϑ and φ rings using Jameson's shock detector [110],

$$\sigma_i = \frac{|u_{i-1} - 2u_i + u_{i+1}|}{|u_{i-1}| + 2|u_i| + |u_{i+1}| + \epsilon}, \qquad i = \theta, \varphi, \quad (41)$$

where $u_i, u_{i\pm1}$ represent the field value in the current cell and its neighbours, and ϵ is a small number used to avoid the division by zero in the denominator. If a single cell in a ϑ or φ ring fulfils $\sigma_i \ge 0.95$, we use the Gaussian filter for a given ring and field; otherwise, we use the exponential filter.

Finally, we note that the characteristic speeds for the GRMHD evolution are always less than the characteristic speeds of the spacetime evolution (some gauge modes have speeds of $\sqrt{2}$), and the GRMHD evolution therefore typically allows for larger CFL factors than the evolution of the fCCZ4 variables. We therefore typically choose $\mathcal{L} = 3$ for the metric fields, and $\mathcal{L} = 12$ for the matter fields.

1. Filtering spacetime fields in the presence of BHs

The spacetime evolution in SphericalNR is subject to two algebraic constraints,

$$\bar{\gamma} = \hat{\gamma} \tag{42}$$

$$\bar{\gamma}^{ij}\bar{A}_{ij} = 0, \tag{43}$$

where $\bar{\gamma}$ and $\hat{\gamma}$ are the determinants of the conformally related metric $\bar{\gamma}_{ij}$ and the background metric $\hat{\gamma}_{ij}$, and $\bar{A}_{ij}$ is the conformally related extrinsic curvature, respectively. In the development of the double FFT filter, we noticed that we need to adjust the way these two constraints are enforced when filtering in the θ direction in the presence of BH spacetimes in order to obtain a stable evolution. Usually, at each Runge-Kutta substep in the evolution, we enforce the above constraints by making the following substitutions at all grid points in the domain:

$$h_{\{i\}\{j\}} \rightarrow \left(\frac{\hat{\gamma}}{\bar{\gamma}}\right)^{\frac{1}{3}}(\delta_{ij} + h_{\{i\}\{j\}}) - \delta_{ij}, \tag{44}$$

where δ_{ij} is the Kronecker delta, and

$$\bar{A}_{\{i\}\{j\}} \rightarrow \bar{A}_{\{i\}\{j\}} - (\delta_{ij} + h_{\{i\}\{j\}})\frac{\bar{\gamma}^{ij}\bar{A}_{ij}}{3}, \tag{45}$$

where we again follow the notation of [34], namely that indices in curly braces represent components in the orthonormal basis with respect to the spherical background metric, whereas normal indices represent components in the coordinate basis.

Enforcing the algebraic constraints this way turned out to be unstable in the presence of BH spacetimes when filtering in the θ direction close to the center of a BH (regardless if we evolve initial data containing BH initial data or in situations where a BH is dynamically formed during evolution, such as the collapse of a NS).

To remedy this instability, we adapt the way we enforce the algebraic constraints as follows: in regions where we need to apply the filtering in the θ direction for CFL stability and the lapse $\alpha < 0.3$, we enforce the constraint (42) as follows (see also [111]):

$$h_{\{1\}\{1\}} = (\hat{\gamma} + \bar{\gamma}_{12}^2\bar{\gamma}_{33} - 2\bar{\gamma}_{12}\bar{\gamma}_{13}\bar{\gamma}_{23} + \bar{\gamma}_{13}^2\bar{\gamma}_{22})$$
$$/(\bar{\gamma}_{22}\bar{\gamma}_{33} - \bar{\gamma}_{23}^2)/(\hat{\mathcal{R}}_{\{1\}}\hat{\mathcal{R}}_{\{1\}}) - 1, \tag{46}$$

where $\hat{\mathcal{R}}_{\{i\}}$ are the rescaling factors of the spherical background metric (see [34]), and we do not enforce the constraint (43) at all. Note that we relaxed the enforcement of the algebraic constraints only inside the horizon.

B. Filtering parallelization

Here we describe the algorithm that we use to perform the FFT filtering across multiple compute nodes. To start, we note that there are two strategies to implement MPI-parallelized FFT filtering: we could either use the parallel FFTW3 [108] implementation; or gather data to be filtered, use serial FFTs to filter, and broadcast the filtered data back to their corresponding MPI ranks. We have chosen the second approach here, rather than relying on a particular parallel implementation of the FFTW3 library being installed on a given cluster. Note that even if we were to use the parallel implementation of FFTW3, we would still need to perform the MPI communicator split described below.

We first split the global MPI communicator in the r direction into a set of smaller communicators: COMM$_r$. In each group COMM$_r$, all the member processes share the same r-coordinate range. Then we split each COMM$_r$ further into two separate groups of communicators: COMM$_{r\theta}$, which all share the same r and θ ranges, and COMM$_{r\varphi}$, which share the same r and φ ranges (see Fig. 1).

The computational domain contained in COMM$_{r\theta}$ covers $0 \leq \varphi < 2\pi$. Because we need to extend the domain in θ to $0 < \theta < 2\pi$, we copy data from processes with $\varphi < \pi$ to the corresponding processes, which owns $\varphi + \pi$ within the given communicator. At this point, processes in COMM$_{r\theta}$ contain both the data corresponding to $0 < \theta < \pi$ and the data corresponding to $\pi < \theta < 2\pi$.

To filter in the φ direction, we use MPI scatter / gather operations to redistribute the data so that each MPI process in COMM$_{r\theta}$ contains a roughly equal number of arrays containing the full set of φ points for some fixed values of r and θ. Each process then performs FFTs on these arrays (multiple FFTs at a time using OPENMP), filters the
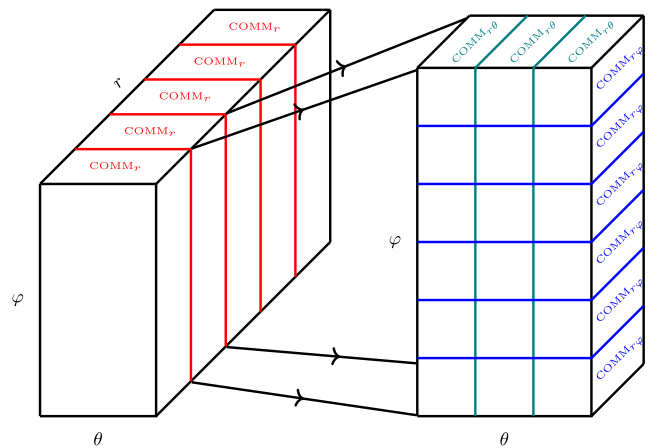

FIG. 1. Overview of the different MPI communicator groups. The global communicator is split along the r direction, and then each r group is split in two different subgroups. For one subgroup, the second splitting is in the θ direction, while for the other, it is in the φ.

transforms, and performs an inverse FFT. The filtered fields are then redistributed back to the original processes in the communicator. Filtering on θ proceeds in much the same way. However, since we use double covering, only half of the rings need to be transformed (i.e., one FFT—filter—inverse FFT operation actually filters two different θ *rings*), only half of the MPI processes need to perform the filtering (we could redistribute the data again so that all MPI processes can perform FFTs, but this would be less efficient due to the extra communication overhead).

In Fig. 2, we show the strong scaling performance of SphericalNR with FFT filtering performed on the Frontera supercomputer at the Texas Advanced Computing Center. Here, we use a grid of $n_r = 256, n_\theta = 128, n_\varphi = 256$ points and increase the number of cores from 64 to 4096. We consider both the performance of the parallel filter and unfiltered algorithm. The unfiltered algorithm requires a time step that is ~136 smaller than the filtered algorithm. When comparing just the number of iterations per unit wall time, we see that overhead of filtering is negligible up to about 300 cores. At 4096 cores, the nonfiltered algorithm is a factor of 1.38 faster in terms of time steps per unit wall time. Of course, when including the severe CFL limitations of the unfiltered algorithm (bottom panel of Fig. 2), we see that the filtered algorithm is actually roughly 100 times

TABLE I. The number of MPI processes in each direction and number of threads per MPI process used for the strong scaling test reported in Fig. 2.

N_{core}	N_r	N_θ	N_φ	Threads
64	8	2	4	1
128	8	4	4	1
256	8	4	8	1
512	8	4	8	2
1024	16	4	8	2
2048	16	4	8	4
4096	16	8	16	2

faster (in terms of physical time) at 4096 cores. In Table I, we list the number of MPI in each direction and threads used for the scaling test.

III. RESULTS

A. Vacuum spacetime test

To evaluate the robustness of our new filtering algorithm, we simulate the same physical BH system previously used in [29] to introduce our new code. The system consists of a single spinning Bowen-York BH [112] (note that, unlike a Kerr BH, a spinning Bowen-York BH contains radiation due to the initial data being conformally flat). We consider two physically equivalent scenarios: one in which the spin is aligned with the polar (z) axis, and another in which the spin is aligned with the y axis. In [29], we were able to show that when extracting the gravitational waves of the BH ringdown via the Weyl scalar Ψ_4, all modes up through $\ell = 8$ were obtained with high accuracy for the aligned spin case. In these earlier results, we used excision techniques to eliminate the severe CFL limitation of the origin in spherical coordinates. Here, we repeated those runs with filtering, rather than excision. While the two configurations are physically equivalent, they require significantly different numerical grid choices. For the case of the z aligned spins, there is no azimuthal variation of the fields, whereas in the y—aligned case, a high azimuthal resolution is required. Consequently, in the y case, the CFL limitations associated with the polar axis are important. For reference, the CFL limitation for an excision run is $dt < r_{exc} \sin(\theta_0/2) d\varphi$, where r_{exc} is the excision radius and θ_0 is the θ grid point closest to the pole.

The initial data were obtained using the TWOPUNCTURES code [113] (the mass, spin, and momentum parameters of one horizon were set to zero). The parameters associated with the data are a bare mass of $1M$ and a spin angular momentum of $0.8M^2$. This corresponds to a BH with a horizon mass of $M_H = 1.1811M$ and a dimensionless spin of $\chi = 0.5735$. We use the AHFinderDirect thorn [114,115] to find apparent horizons (AHs) [116] and the QuasiLocalMeasures thorn [117,118] to calculate the angular momentum of the apparent horizon during the evolution. The BH spin is
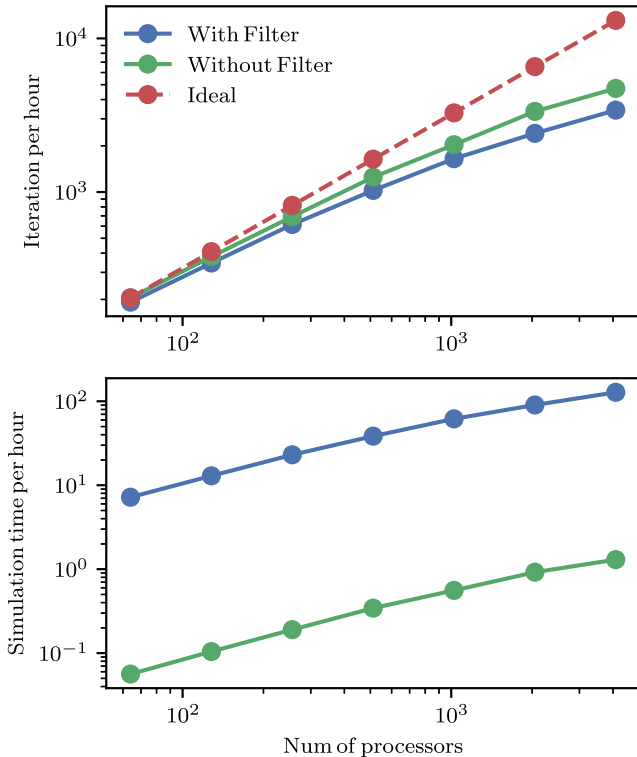

FIG. 2. Strong scaling of SphericalNR with the FFT filtering scheme. In the top plot, we show iterations per hour for both the code with and without the FFT filter. The code without the filter requires a time step 1/136 as small as with filtering. The bottom plot shows the actual performance in run time versus wall time.

TABLE II. The grid parameters for all simulations. Here n_r, n_θ, and n_φ are the number of grid points in the radial, polar, and azimuthal directions, respectively, and dt is the time step.

	n_r	n_θ	n_φ	dt
Aligned(64)	2500	64	4	0.00490
Aligned(96)	3750	96	4	0.00327
FFT(64)	2500	64	128	0.001
FFT(96)	3750	96	192	0.00067

measured using the flat space rotational Killing vector method [119] that was shown to be equivalent to the Komar angular momentum [120] in foliations adapted to the axisymmetry of the spacetime [121].

We denote the simulations by Aligned(XX) and FFT (XX), where XX refers to the number of polar grid points, aligned and FFT refer to simulations where the spins are aligned with the polar axis and nonaligned with the polar axis (hence, both the θ and φ FFT filters are needed). Note that the aligned cases were performed using excision of the BH interior (hence, no filtering of any kind was used).

In Table II, we give the parameters for the computational grids used in all the simulations. For these runs, we set the filtering parameter $\mathcal{L}$ to $\mathcal{L} = 2$.

In Fig. 3, we show the L^2 norm of the Hamiltonian constraints for $n_\theta = 64$ and $n_\theta = 96$ for the using FFT filter case. After the initial oscillation, the constraint violation settles down to 7×10^{-7} and 3×10^{-7} for $n_\theta = 64$ and $n_\theta = 96$, respectively.

In Fig. 4, we show the algebraic constraints violation (43) and Hamiltonian constraints along $\theta = d\theta/2, \varphi = 0$ at $t = 150M$. The region where we do not enforce the algebraic constraints is within the horizon. All points on the horizon, and outside, have the algebraic constraints enforced. As we
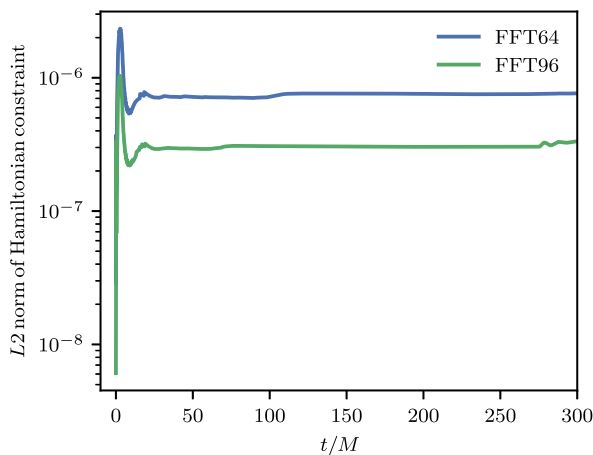

FIG. 4. Algebraic constraints (43) and Hamiltonian constraints along $\theta = d\theta/2, \varphi = 0$ at $t = 150M$ for case FFT96. The vertical line indicates the radius of apparent horizon.

can see, the algebraic constraint violations remain below 10^{-13} even at radius of $r \sim 0.35$ (here, the horizon radius is at $r = 0.915$). The algebraic constraint do increase closer to the puncture to about 1.0. However, this violation is nonpropagating.

In Fig. 5, we show the evolution of the irreducible mass M_{irr}. After having absorbed some of the initial junk radiation, M_{irr} should remain constant absent of numerical errors (constraint violations occurring in free evolution can act as negative mass and result in an unphysical reduction of M_{irr} [122–124]). We see that the nonaligned case using the double FFT filter rapidly converges to the M_{irr} obtained in the aligned case, our reference point. In Fig. 6, we show that the higher-order waveforms mode for the nonaligned case agree very well with the aligned case. Here, we rotate

FIG. 3. The L^2 norm of the Hamiltonian constraints versus time at two resolutions FFT64 and FFT96. Here, the norm only includes points outside the horizon. The drop in constraint magnitude between FFT64 and FFT96 is consistent with a convergence order of 2.
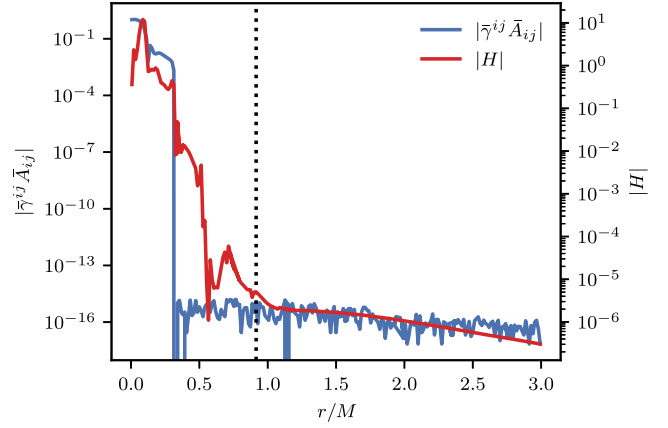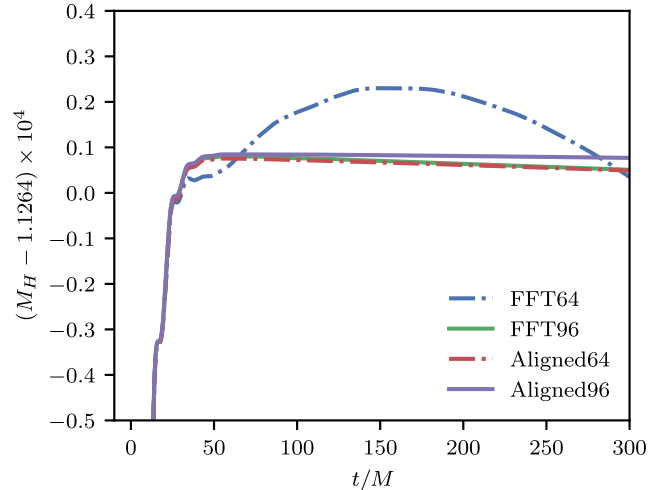

FIG. 5. A comparison of the irreducible mass of the BH versus time as measured by AHFinderDirect for $n_\theta = 64$ and $n_\theta = 96$ for the aligned case and using the double FFT filter. Here, mass conservation would imply that the irreducible mass settles to a constant value.
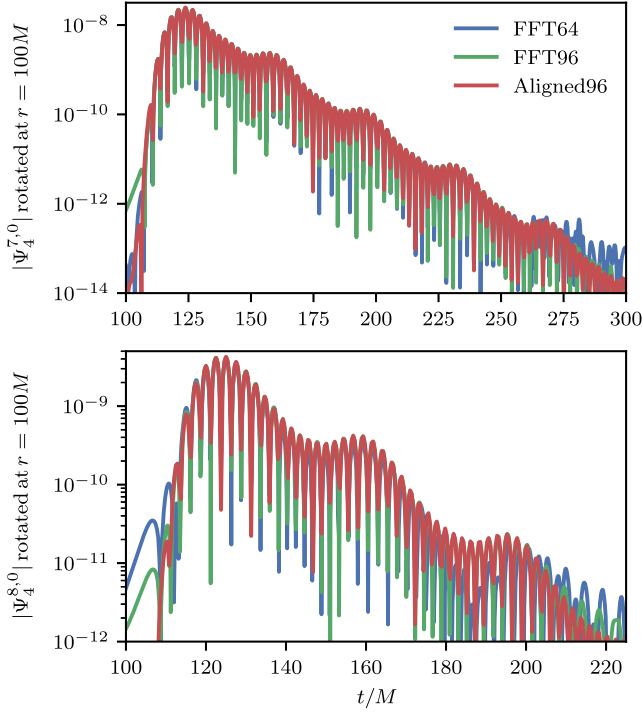
FIG. 6. A comparison of the $\ell = 7$ and $\ell = 8$ modes of Ψ_4.

all waveforms of the nonaligned cases to a frame where the z axis is aligned with the spin axis so that they should reproduce the aligned waveform. In this frame, only the $m = 0$ modes are nontrivial in the continuum limit. The aligned96 run is expected to have the smallest error, and we see that the double FFT filter runs rapidly converge to it. Note that differences are only apparent for the last few cycles.

B. GRMHD tests

1. Off-center spherical explosion

To evaluate the effectiveness of our new filtering algorithm in solving challenging relativistic MHD problems, we selected the same test case as in our previous study [34]: a spherical explosion [125], but with the explosion center intentionally displaced from the origin. The initial data consist of an overdense ($\rho = 1 \times 10^{-2}$, $p = 1.0$) ball of radius 1.0. From a radius of 0.8 outwards, the solution is matched in an exponential decay to the surrounding medium ($\rho = 1 \times 10^{-4}$, $p = 3 \times 10^{-5}$). We use a Γ—law equation of state (EOS) with $\Gamma = 4/3$. The entire domain is initially threaded by a constant magnitude magnetic field ($B^z = 0.1$). The fluid three-velocity is set to zero everywhere in the domain initially. We use a fixed background Minkowski spacetime for this test problem. In order to remove any symmetries in the initial data and test the double FFT filtering in a full 3D setting, we offset to the center of the overdense region to $(x = 1.1, y = 0, z = 0)$

and rotate the magnetic field by 45° about the x axis initially; the shock front of the explosion will therefore have to pass through the origin and polar axis.

We use $(n_r = 160, n_\theta = 80, n_\varphi = 160)$ points, with the outer boundary $r_{max} = 6.0$, and use the double FFT filter to increase the time step from $dt = 7 \times 10^{-6}$ (stable limit without filtering) to $dt = 1 \times 10^{-3}$. Here, we use the filtering parameter $\mathcal{L} = 4$. We use MPWENO-Z9, as we found that the MP limiter helps the shock pass through origin and axis, tenth order finite differences in the curl of A_i, ninth order KO dissipation with a dissipation strength $\epsilon_{\mathrm{diss}} = 0.1$, global Lax-Friedrich fluxes with higher order flux corrections, and isotropic floors with $\rho_{\mathrm{floor}} = 1 \times 10^{-7}$, $(\rho\epsilon)_{\mathrm{floor}} = 1 \times 10^{-9}$.

The final distribution at $t = 4$ for the pressure P (in the $x = 1.1$ and $y = 0$ planes) is shown in Fig. 7. Here, we do see the shock front propagating through the origin and poles, but there are small residual artifacts associated with them. The test is particularly challenging here because radial flows near the origin need to be converted into angular flows around the origin (the lower radial face there would have size of zero). A similar complication arises on the poles when considering longitudinal flows. In this test, we see that while the magnetized shock largely passes through the origin and axes, there are visible artifacts. The shock front propagation through the origin is slightly delayed, leading to a bump on the shock front. There is also extra pressure in the vicinity of the pole which is the result of occasional primitive recovery failures, which is not unexpected, as the difficulty of this test lies in the primitive recovery [126]. We note that we performed a similar test in a previous paper [34], filtering only in the φ direction (with a correspondingly smaller time step than used here) and used lower-order reconstruction methods. With the improvements to the robustness of our GRMHD code described in Sec. II above, SphericalNR is now able to evolve the off-center spherical explosion using higher order methods.

2. Off-center neutron star

Next, we turn to the dynamical spacetime evolution of NSs, testing the double FFT filter in the coupled spacetime and GRMHD evolution. Our first test is the evolution of a stable rotating NS. We evolve model B2 of [127] and add a weak poloidal magnetic field initially. Similar to the spherical explosion, we place the center of the star off center at $(x, y, z) = (1, 1, 0)$ initially. The fluid and spacetime initial data are generated with the RNS code [128], which has been incorporated as the Hydro_RNSID thorn in the Einstein Toolkit.

Model B2 is differentially rotating and is described by a j-law profile,

$$\Omega_c - \Omega = \frac{1}{\hat{A}^2 R_e^2} \left[\frac{(\Omega - \omega)r^2 \sin^2\theta e^{-2\nu}}{1 - (\Omega - \omega)r^2 \sin^2\theta e^{-2\nu}} \right], \quad (47)$$
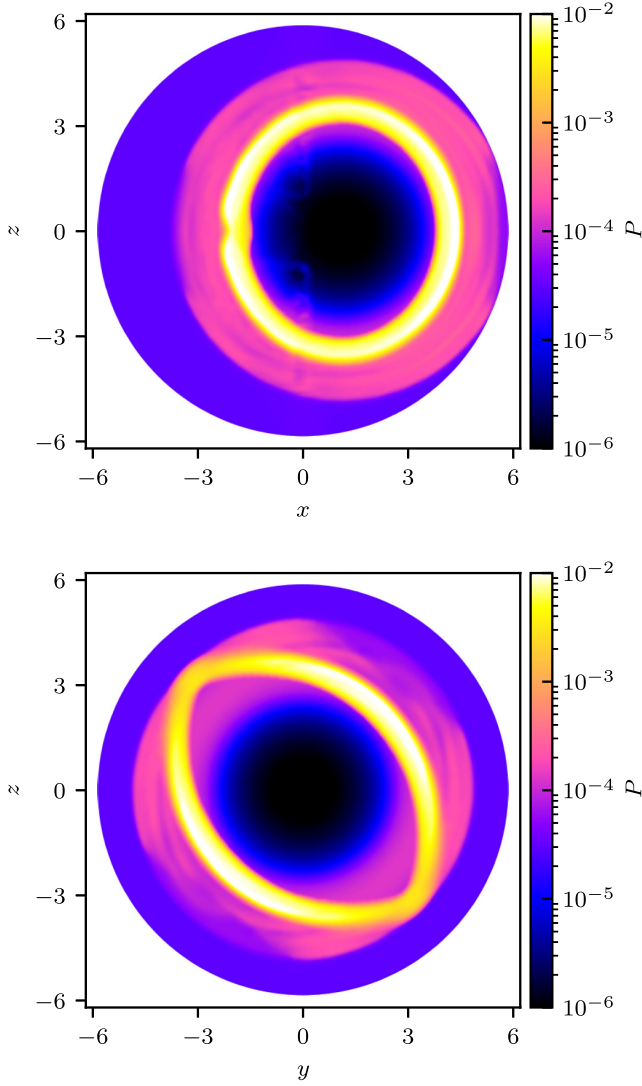
FIG. 7. Pressure in the x-z and y-z plane at $t = 4$, with initial magnetic field $B^z = 0.1$ rotated by 45° about x axis. The top panel shows the shock front along the xz plane ($y = 0$), while the bottom shows the shock front on the plane $x = 1.1$ (note that the center of the explosion is at $x = 1.1$). The bottom panel show the $x = 1.1$ plane (the shock is centered along $x = 1.1$). The flow morphology is clearly seen to be tilted by 45°.

where R_e, Ω_c are provided in Table III, and $\hat{A}$ is a measure of the degree of differential rotation, which we set to $\hat{A} = 1$. After interpolating and coordinate transforming the fluid and spacetime data from Hydro_RNSID to the orthonormal basis in spherical coordinates, we add a weak poloidal magnetic field, following the vector-potential-based prescription of [16]:

$$A_x = -(y - y_c)A_b \left(1 - \frac{\rho}{\rho_c}\right)^{n_s} \max(P_{\text{cut}} - P, 0), \quad (48)$$

$$A_y = (x - x_c)A_b \left(1 - \frac{\rho}{\rho_c}\right)^{n_s} \max(P_{\text{cut}} - P, 0), \quad (49)$$

TABLE III. Main properties of the relativistic polytrope models B2 [127] and U11 [129]: central rest-mass density ρ_c, rest- and gravitational masses M_0 and M, the dimensionless angular momentum J/M^2, the proper equatorial radius R_e, the angular velocities at the axis Ω_c and at the equator Ω_e, the ratio of polar and equatorial radii of the star r_p/r_e, the ratio of kinetic energy and gravitational binding energy $T/|W|$, the adiabatic index Γ, the polytropic constant K, and the constants prescribing the initial magnetic field A_b, n_s and P_{cut} (see main text for details).

	B2	U11
ρ_c	1.28×10^{-3}	1.092×10^{-4}
M_0	1.592	1.508
M	1.478	1.462
J/M^2	3.177×10^{-1}	1.660
R_e	9.92	23.3
Ω_c	1.53×10^{-2}	1.29×10^{-2}
Ω_e	9.45×10^{-3}	8.61×10^{-3}
r_p/r_e	0.900	0.250
$T/|W|$	2.574×10^{-2}	2.743×10^{-1}
Γ	2	2
K	100	100
A_b	10	10
n_s	3	2
P_{cut}	6.542×10^{-6}	9.083×10^{-8}

$$A_z = 0, \quad (50)$$

$$\varphi = 0, \quad (51)$$

where values of A_b, ρ_c, n_s, and P_{cut} are provided in Table III. This choice of initial vector potential in Cartesian coordinates results in a purely azimuthal vector potential and therefore, a purely poloidal magnetic field. A_i is then transformed to the orthonormal basis in spherical coordinates, and the initial magnetic is calculated from the curl of A_i. While the EOS of the initial data are polytropic, we evolve the star with a Γ-law EOS with $\Gamma = 2$. We use SSPRK54 for time integration, fourth order finite differences with fifth order KO dissipation with $\epsilon_{\text{diss}} = 0.01$ in the spacetime evolution, the HLLE Riemann solver, WENO-Z9 reconstruction, tenth order finite difference in the curl of A_i, ninth order KO dissipation with $\epsilon_{\text{diss}} = 0.01$, isotropic floors with $\rho_{\text{floor}} = 5 \times 10^{-9}$, $(\rho\epsilon)_{\text{floor}} = 5 \times 10^{-11}$, $W_{\text{max}} = 50$, and $\epsilon_{\text{max}} = 1$. We evolved this off-centered NS configuration using four different resolutions: $n_r \times n_\theta \times n_\varphi = 256 \times 16 \times 32 (h_0)$, $512 \times 32 \times 64 (h_1)$, $768 \times 48 \times 96 (h_2)$, and $1024 \times 64 \times 128 (h_3)$.

Since the NS is not centered on the origin, truncation errors introduce asymmetries into its evolution. Consequently, the NS drifts from its starting position (where it would remain if the grid was adapted to the symmetries of the star). Based on the results from our previous test, matter flows through the origin are impeded relative to flows across nonsingular points. Therefore, it is
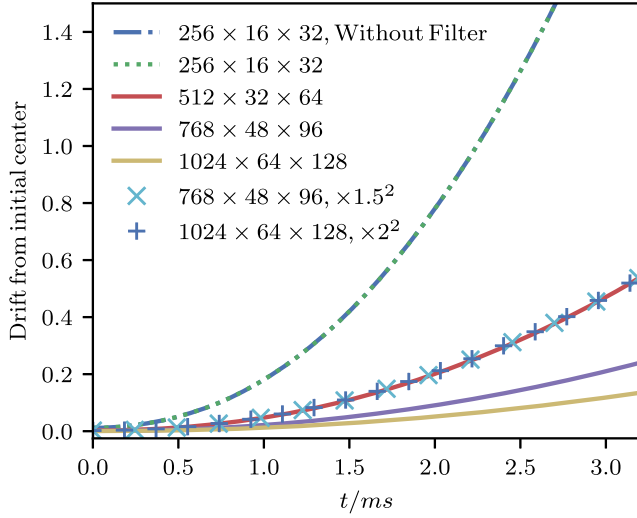
FIG. 8. Drift of the NS center of mass for different resolutions. The plot shows relative drift of the center of the NS for four different resolutions: $h_0(256 \times 16 \times 32)$, $h_1(512 \times 32 \times 64)$, $h_2(768 \times 48 \times 96)$, $h_3(1024 \times 64 \times 128)$. The crosses show the relative drift of the h_2 run after rescaling by the square of the ratio of the h_2 to h_1 resolution grid sizes. The pluses show the same rescaled drift but for the h_3 case. These rescaled drifts show clear second-order convergence. The dashed and doted curve are two h_0 resolution runs with and without filtering. They are on top of each other showing that the filter has no effect on the drift of the NS.

not apparent *a priori* that the drift will consistently converge to zero with increased resolution.

In Fig. 8, we show that the drift of the NS from its initial location converges to zero to second order. In the figure, the cross and plus symbols show the drift of the h_2 and h_3 resolutions overlap with the h_1 resolution drift if the former two are multiplied by the square of the ratio of their resolutions to the h_1 resolution. (Note that although we use higher-order reconstruction, the main algorithm is still second-order convergent). This indicates that the errors associated with flows through the singular regions do converge away.

Figure 9 shows the relative error in the conservation of total rest mass in the domain. As explained in [34], our implementation of the continuity equation in the reference metric formalism does not conserve total rest mass to round-off, but the total mass loss/gain will converge to zero with increasing resolution (additionally, some of the fixes in the primitive recovery and the need to use an artificial atmosphere will also break conservation of total rest mass). The plot shows several points on the h_2 and h_3 resolution curves after multiplying by the inverse of the ratio of the h_2/h_3 resolution with the h_1 resolution raised to the power of 2.76 (i.e., demonstrating between second and third-order convergence).

The evolution of the fractional change in the maximum density is shown in Fig. 10. Truncation errors in the
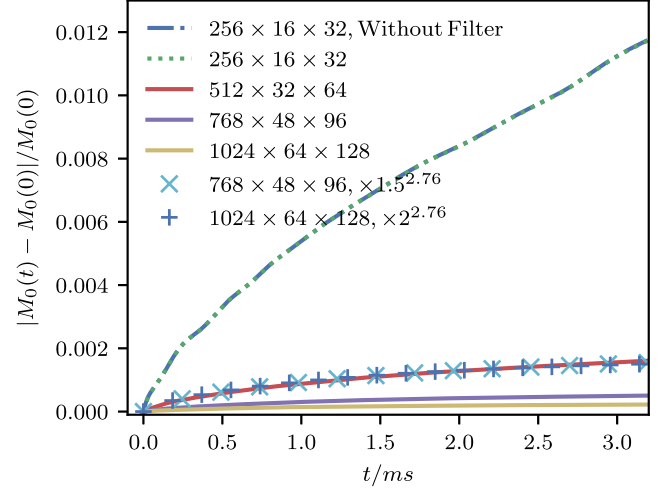

FIG. 9. Conservation of total rest mass for different resolutions. The plot shows relative change in the total mass of the NS for four different resolutions: $h_0(256 \times 16 \times 32)$, $h_1(512 \times 32 \times 64)$, $h_2(768 \times 48 \times 96)$, $h_3(1024 \times 64 \times 128)$. The crosses show the relative change in mass of the h_2 resolution run after rescaling by the ratio of the h_2 to h_1 resolution grid sizes to the power 2.76. The pluses show the same rescaled mass change, but for the h_3 case. Hence, the convergence order is between 2 and 3. The dashed and doted curve are two h_0 resolution runs with and without filtering. They are on top of each other showing that the filter has no effect on the conservation of total rest mass.

spacetime evolution, the interface of the NS surface and atmosphere as well as the asymmetric grid in our setup introduce perturbations of the NS that cause the central density to oscillate. As model B2 is stable, these should
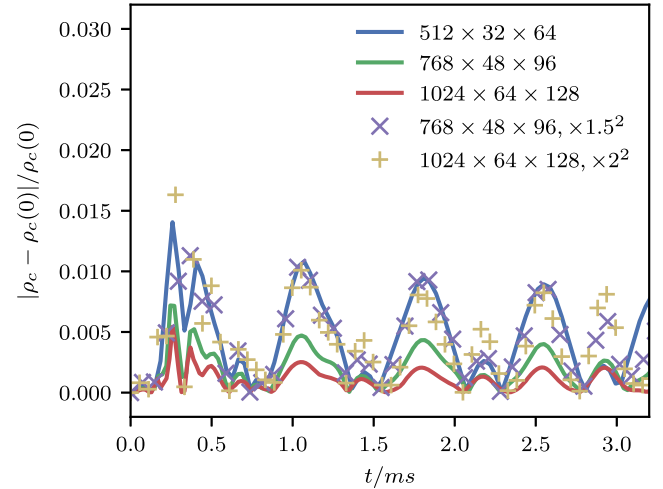

FIG. 10. Maximum density versus time for different resolutions. The plot shows relative change in the central density of the NS versus time for three different resolutions. The crosses show the relative change of the h_2 resolution run after rescaling by the square of the ratio of the h_2 to h_1 resolution grid sizes. The pluses show the same rescaled change, but for the h_3 resolution case. In regions where the relative change in the central density is large, second-order convergence is observed.
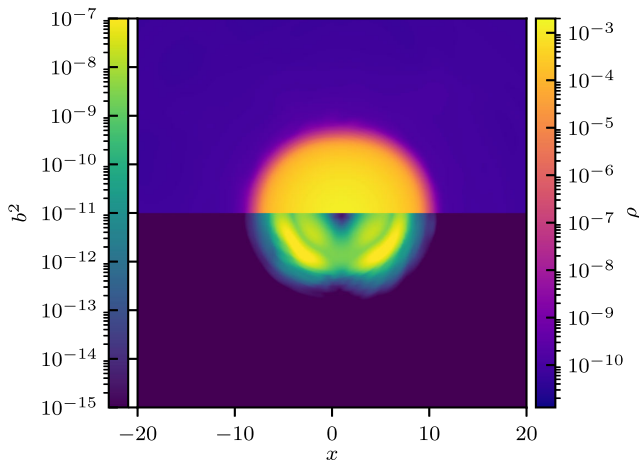
FIG. 11. ρ and b^2 evolution in $x-z$ plane of $y=1$ of model B2 at $t=3$ ms.

converge away with grid resolution in the absence of added perturbations. The convergence of the oscillations of the central density is less clean than either the drift or the total mass, likely due to the h_1 resolution case being too low. Here, we see that the oscillations generally converge away at second-order when the perturbations are large.

Finally, Fig. 11 shows the distributions of ρ and b^2 in the $y=1$ plane at $t=3$ ms. The star remains stable and the stellar surface is well captured by the code. During the evolution, the quantity b^2 develops a richer morphology than it had at the beginning. This test shows that the double FFT filter method works in a setup not adapted to the symmetries of the coordinate system in a dynamical spacetime and GRMHD evolution.

3. Dynamical bar-mode instability

Our final code test serves as a proxy for the postmerger remnant of a binary NS merger: the evolution of the dynamical bar-mode instability of a NS in a dynamical spacetime [130] (see also the reviews in [131,132]). We evolve the dynamical bar-mode instability in model U11 from [129]. The initial data configuration is outlined in Table III. To generate the initial NS, we use again the Hydro_RNSID thorn and place the star at the origin and such that its spin axis is aligned with the polar axis. To trigger the growth of the bar-mode instability, we perturb the pressure by 5% with random noise initially. We add an initial poloidal magnetic field determined by Eqs. (48)–(51), setting $x_c = y_c = 0$ since the star is initially centered on the coordinate origin. The constants A_b, n_s, and P_{cut} are chosen in such a way that $b_{\text{max}}^2(t=0) \approx 1 \times 10^{15} G$, which is classified as moderate field strength in [129], where it was shown that such a magnetic field is not strong enough to suppress the development of the bar-mode instability.

We use SSPRK54 for time integration, fourth order finite differences with fifth order KO dissipation with

$\epsilon_{\text{diss}} = 0.05$ in the spacetime evolution, the HLLE Riemann solver, WENO-Z9 reconstruction, tenth order finite difference in the curl of A_i, ninth order KO dissipation with $\epsilon_{\text{diss}} = 0.001$, $W_{\text{max}} = 50$, $\epsilon_{\text{max}} = 1$, and radially dependent floors with $\rho_{\text{floor}} = 1 \times 10^{-19}$, $(\rho\epsilon)_{\text{floor}} = 1 \times 10^{-24}$, and $r_{\text{min}} = 20$. The improvements made to our primitive recovery scheme described in Sec. II allow us to use these very low floor values and still stably evolve the magnetic field everywhere in the domain.

In Fig. 12, we show snapshots of both b^2 and ρ in the xy and xz planes at select times: prior to the onset of the bar-mode instability, the fully developed bar-mode including spiral arms, and at late times when the NS has become nearly axisymmetric again and is now surrounded by a disk with a turbulent magnetic field as a result of the growth of the magnetorotational instability [133–136]. To quantify the development and subsequent saturations of the bar-mode instability, we plot the time evolution of the azimuthal Fourier modes of ρ,

$$D_m = \int \alpha\sqrt{\gamma}\rho e^{-im\varphi} d^3x, \tag{52}$$

in Fig. 13. The evolution is very similar to the results of [129,137] (see in particular the schematic of mode evolution shown in Fig. 8 in [137]). As observed in [129], the chosen initial magnetic field is not strong enough to disrupt the dynamical bar-mode instability.

To test the correctness of the coupled spacetime and fluid evolution, we also plot the $(\ell = 2, m = 2)$ mode of the Weyl scalar Ψ_4 in Fig. 13 to compare it compare it with D_2. The idea here is that $\ell = 2$, $m = 2$ quadrupole moment of the gravitational waveform should be dominated by the azimuthal $m = 2$ mode of the density distribution. This, in turn, should be the dominant contribution to the gravitational wave signal. As seen in Fig. 13, the two modes are strongly correlated (after accounting for a time translation of $t = 1600$ due to the distance to where we extract Ψ_4, as well as an arbitrary factor to make it easier to see that both curves have the same growth rate).

In Fig. 14, we plot the "toroidal" component of the magnetic energy [129],

$$E_{\text{mag}}^{\text{tor}} = \int \sqrt{\gamma}\frac{1}{2}B_\parallel B_\parallel d^3x, \tag{53}$$

where $B_\parallel = B^j v_j / (v^i v_i)^{1/2}$ is the "parallel" part of the magnetic field along the direction of the fluid motion. Note that v^i is the Valencia 3-velocity, and the indices are raised and lowered with the spatial metric γ_{ij}. At early times, when the bar-mode has not yet developed, the differential rotation profile of NS winds up the poloidal magnetic field; therefore, the toroidal magnetic energy is expected to grow quadratically with time (i.e., $\sqrt{E_{\text{mag}}^{\text{tor}}} \propto t$) [129,138]. Here, we performed runs at four different resolutions and
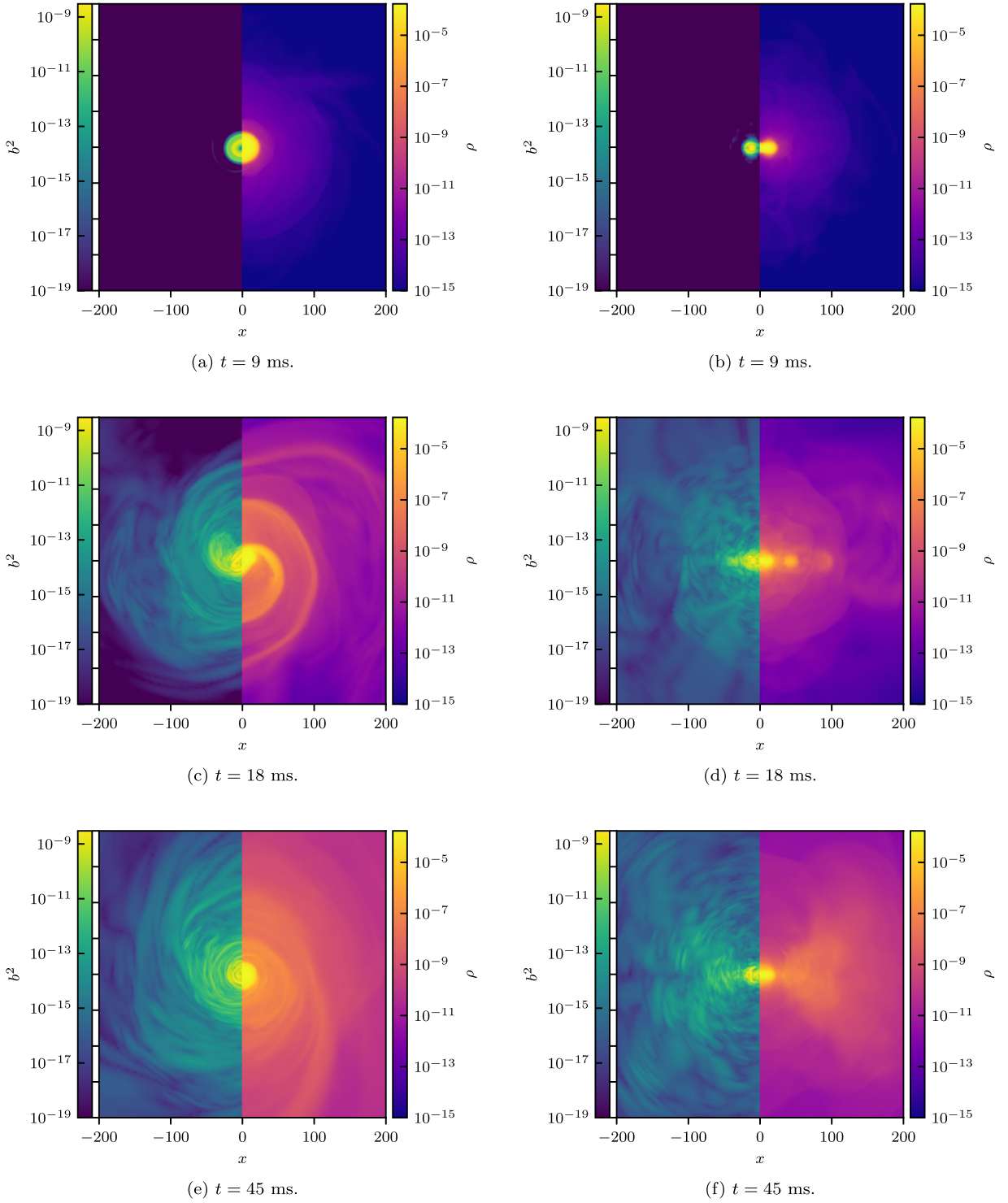
(a) $t = 9$ ms.   (b) $t = 9$ ms.

(c) $t = 18$ ms.   (d) $t = 18$ ms.

(e) $t = 45$ ms.   (f) $t = 45$ ms.

FIG. 12. Snapshots of b^2 and ρ on $x - y$ (left column) and $x - z$ (right column) plane of model U11 at $t = 9$ ms (top row), $t = 18$ ms (middle row), and $t = 45$ ms (bottom row).

measured the growth of this energy. We find that the toroidal component of the energy converges between first and second order. We plot $E_{\mathrm{mag}}^{\mathrm{tor}}$ for the four resolutions and a Richardson extrapolation of these results in Fig. 14. Prior to the onset of the bar-mode (i.e., for $t \lesssim 10$ ms), the

Richardson extrapolated $E_{\mathrm{mag}}^{\mathrm{tor}}$ grows as t^2 (i.e., has a slope of 2 on a log-log plot), with the lower resolution simulations exhibiting successively smaller exponents, showing that the code converges to the expected behavior. The lowest resolution run ($256 \times 16 \times 32$) was run with and
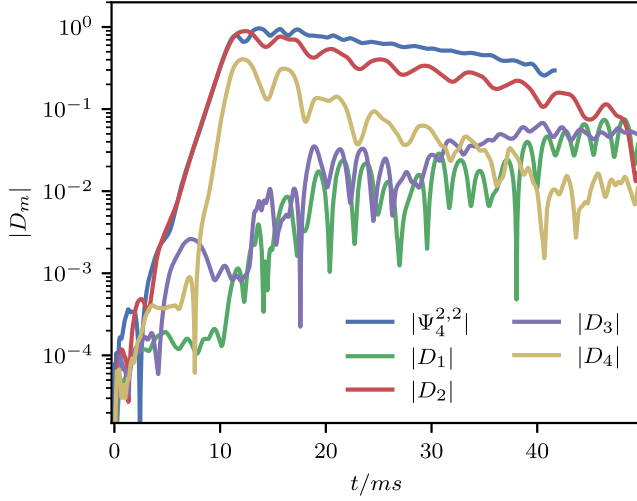
FIG. 13. Evolution of the first four nonaxisymmetirc matter distribution modes and the $(\ell = 2, m = 2)$ mode of Ψ_4. As expected, the $m = 2$ mode of the density distribution is the dominant contribution to the waveform quadrupole mode.

FIG. 15. The L^2 norm of the Hamiltonian constraint for the bar-mode-unstable star. Prior to the onset of the bar-mode instability, we see convergence (to zero) at 1.5 order. Note that, after the onset of the instability (which is seeded by random perturbations), the constraint violations remain small and do not exhibit exponential growth.

without the filter. Since there is no visible difference in the toroidal magnetic energy growth when the filter is added or removed, this indicates that truncation error dominates over any errors introduced by the filter.

In Fig. 15, we show the L^2 norm of the Hamiltonian constraint for the three resolutions. Note that the onset of

FIG. 14. The toroidal component of the magnetic energy E_{mag}^{tor} for early times and different resolutions. Prior to the formation of the instability, the magnitude of the E_{mag}^{tor} is expected to increase quadratically in time [129,138] (i.e., as t^2). The plot shows E_{mag}^{tor} for different resolutions and a Richardson extrapolations assuming second-order convergence, as well as quadratic curve $y = ct^2$ (chosen to match the initial behavior of the Richardson extrapolated curve). The lowest resolution run ($256 \times 16 \times 32$) was run with and without the filter. Since there is no visible difference in the toroidal magnetic energy growth when the filter is added or removed, this demonstrates that truncation error dominates over any errors introduced by the filter.
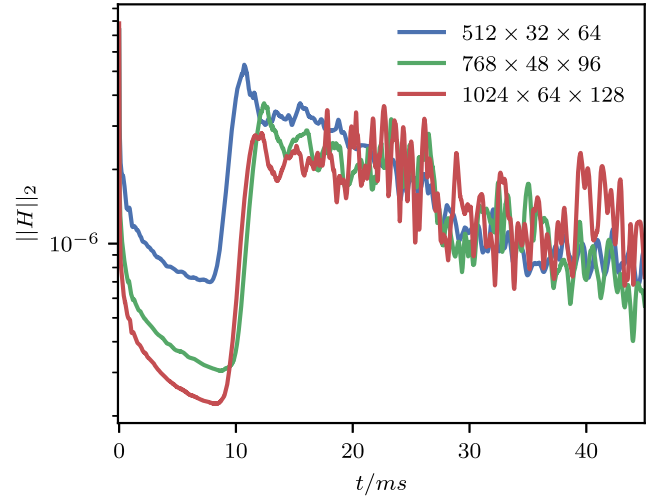
the bar-mode instability is triggered by random perturbations, so the time of this blowup is not expected to converge. Prior to the onset, we do see convergence of the constraints (except at $t = 0$, where the constraint violations due to the initial perturbations dominate). Note that the constraint violations, after the initial bar-mode instability starts, remain roughly constant (with a small damping in time due to the constraint damping of the fCCZ4 spacetime evolution system).

IV. DISCUSSION

Spherical coordinates are an attractive choice for GRMHD simulations of systems that possess (approximate) spherical- or axisymmetry, in particular they conserve fluid angular momentum and allow for a lower number of grid points compared to Cartesian coordinates. However, solving hyperbolic partial differential equations in spherical coordinates with high resolution suffers from the well-known CFL limitation resulting in prohibitively small time steps. In this work, we have developed a double FFT filtering algorithm for the coupled evolution of dynamical spacetimes and GRMHD in the SphericalNR/ Einstein Toolkit framework to ameliorate these CFL limitations by filtering both great circles in θ and coordinate rings in φ depending on radius and latitude. Smooth fields are filtered by exponentially dampening CFL-unstable modes, while a hybrid exponential/Gaussian filter is used to filter fluid fields that can become discontinuous, in order to avoid Gibbs phenomenon when filtering. For these fields, the filter switches automatically between exponential and Gaussian filtering using Jameson's shock detector.

The double FFT filter presented here is fully MPI-parallelized, allowing for domain decomposition in the angular coordinates even though the FFT filter is a global operation (per great circle or azimuthal coordinate ring). Importantly, we showed good strong scaling properties of the algorithm up to thousands of cores. With the new filtering algorithm, we increase the time step from $dt \sim dr/2 \sin(\pi/(2n_\theta))2\pi/n_\varphi$ to a time step using effective $n_\theta < 10$ and $n_\varphi < 10$, which can result in a time step orders of magnitude larger when filtering in high angular resolution simulations.

We have performed extensive testing of the new SphericalNR code with the double FFT filter both in vacuum spacetimes and spacetimes coupled to GRMHD to evaluate its robustness and effectiveness. We performed code tests in which we deliberately subject the SphericalNR with filtering to situations not adapted to the spherical coordinate system: the evolution of a Bowen-York BH with its spin axis aligned with the y axis, and off-center simulations of a magnetized spherical explosion and a stable magnetized NS. These tests require significantly more angular resolution in the φ coordinate than their counterparts when adapted to the symmetries (all three problems are axisymmetric) to produce accurate results. For the vacuum test, we repeated the vacuum spacetime test of the original implementation of SphericalNR [29], showing that the FFT filtering is able to quickly achieve convergence to the expected results for spinning Bowen-York BHs, comparing to the axisymmetric result when the spin is aligned with the z axis. Next, we successfully tested our new implementation by performing two challenging off-center GRMHD simulations: an off-center spherical explosion and the evolution of an off-center magnetized stable NS. Our code was able accurately reproduce known results and shown the expected convergence.

Finally, we evolved a magnetized NS model that is unstable against the dynamical bar-mode instability. This test was chosen as the dynamical bar-mode formation and saturation mimics the late stages of a BNS merger forming spiral arms and settling to a stable NS surrounded by a hot accretion disk. This test showed convergence and the correct coupled evolution of the dynamical spacetime and matter by showing a clear correlation between the growth rate of the $m = 2$ azimuthal Fourier mode in the density distribution and the $\ell = 2$, $m = 2$ mode of the Weyl scalar Ψ_4. This type of test is important to show that SphericalNR is capable of very long-term simulations of the postmerger remnant of BNS such as hypermassive NS and BH accretion disks. With our new FFT filtering

algorithm these simulations can be performed in spherical coordinates, while maintaining convergent behavior.

Avoiding the CFL time step limitation with the double FFT filter presented in this work, SphericalNR is well suited to simulate long-term BNS post-merger remnants. While previous studies of BNS postmergers with spherical codes [27] used a fixed metric approach, our framework includes a fully dynamical metric. This will allow us to study the lifetime of hypermassive NS remnants and jet formation, and other interesting astrophysical scenarios, including gravitational core collapse and accretion into single or binary black hole systems.

ACKNOWLEDGMENTS

[1] B. P. Abbott *et al.* (LIGO Scientific and Virgo Collaborations), Phys. Rev. Lett. **116,** 061102 (2016).

[2] B. P. Abbott *et al.* (LIGO Scientific and Virgo Collaborations), Phys. Rev. Lett. **116,** 241102 (2016).

[3] B. P. Abbott *et al.* (LIGO Scientific and Virgo Collaborations), Phys. Rev. Lett. **116,** 241103 (2016).

[4] B. P. Abbott *et al.* (LIGO Scientific and VIRGO Collaborations), Phys. Rev. Lett. **118,** 221101 (2017); **121,** 129901(E) (2018).

[5] B. P. Abbott *et al.* (LIGO Scientific and Virgo Collaborations), Astrophys. J. **851,** L35 (2017).

[6] B. P. Abbott *et al.* (LIGO Scientific and Virgo Collaborations), Phys. Rev. Lett. **119,** 141101 (2017).

[7] B. P. Abbott *et al.* (LIGO Scientific and Virgo Collaborations), Phys. Rev. Lett. **119,** 161101 (2017).

[8] B. P. Abbott *et al.* (LIGO Scientific, Virgo, Fermi GBM, INTEGRAL, IceCube, AstroSat Cadmium Zinc Telluride Imager Team, IPN, Insight-Hxmt, ANTARES, Swift, AGILE Team, 1M2H Team, Dark Energy Camera GW-EM, DES, DLT40, GRAWITA, Fermi-LAT, ATCA, AS-KAP, Las Cumbres Observatory Group, OzGrav, DWF (Deeper Wider Faster Program), AST3, CAASTRO, VINROUGE, MASTER, J-GEM, GROWTH, JAGWAR, CaltechNRAO, TTU-NRAO, NuSTAR, Pan-STARRS, MAXI Team, TZAC Consortium, KU, Nordic Optical Telescope, ePESSTO, GROND, Texas Tech University, SALT Group, TOROS, BOOTES, MWA, CALET, IKI-GW Follow-up, H.E.S.S., LOFAR, LWA, HAWC, Pierre Auger, ALMA, Euro VLBI Team, Pi of Sky, Chandra Team at McGill University, DFN, ATLAS Telescopes, High Time Resolution Universe Survey, RIMAS, RATIR, and SKA South Africa/MeerKAT Collaborations), Astrophys. J. **848,** L12 (2017).

[9] B. P. Abbott *et al.* (LIGO Scientific, Virgo, Fermi-GBM, and INTEGRAL Collaborations), Astrophys. J. **848,** L13 (2017).

[10] M. Shibata and K. ō. Uryū, Phys. Rev. D **61,** 064001 (2000).

[11] F. Pretorius, Phys. Rev. Lett. **95,** 121101 (2005).

[12] M. Campanelli, C. O. Lousto, P. Marronetti, and Y. Zlochower, Phys. Rev. Lett. **96,** 111101 (2006).

[13] J. G. Baker, J. Centrella, D.-I. Choi, M. Koppitz, and J. van Meter, Phys. Rev. Lett. **96,** 111102 (2006).

[14] M. Shibata and K. Uryū, Phys. Rev. D **74,** 121503 (2006).

[15] M. Anderson, E. W. Hirschmann, L. Lehner, S. L. Liebling, P. M. Motl, D. Neilsen, C. Palenzuela, and J. E. Tohline, Phys. Rev. Lett. **100,** 191101 (2008).

[16] Y. T. Liu, S. L. Shapiro, Z. B. Etienne, and K. Taniguchi, Phys. Rev. D **78,** 024012 (2008).

[17] S. Chawla, M. Anderson, M. Besselman, L. Lehner, S. L. Liebling, P. M. Motl, and D. Neilsen, Phys. Rev. Lett. **105,** 111101 (2010).

[18] J. A. Faber and F. A. Rasio, Living Rev. Relativity **15,** 8 (2012).

[19] L. Lehner and F. Pretorius, Annu. Rev. Astron. Astrophys. **52,** 661 (2014).

[20] L. Baiotti and L. Rezzolla, Rep. Prog. Phys. **80,** 096901 (2017).

[21] F. K. Thielemann, M. Eichler, I. V. Panov, and B. Wehmeyer, Annu. Rev. Nucl. Part. Sci. **67,** 253 (2017).

[22] B. D. Metzger, Living Rev. Relativity **23,** 1 (2019).

[23] M. D. Duez and Y. Zlochower, Rep. Prog. Phys. **82,** 016902 (2019).

[24] M. Shibata and K. Hotokezaka, Annu. Rev. Nucl. Part. Sci. **69,** 41 (2019).

[25] L. Baiotti, Prog. Part. Nucl. Phys. **109,** 103714 (2019).

[26] K. Kyutoku, M. Shibata, and K. Taniguchi, Living Rev. Relativity **24,** 5 (2021).

[27] F. G. Lopez Armengol *et al.*, Phys. Rev. D **106,** 083015 (2022).

[28] O. Porth *et al.*, Astrophys. J. Suppl. Ser. **243,** 26 (2019).

[29] V. Mewes, Y. Zlochower, M. Campanelli, I. Ruchlin, Z. B. Etienne, and T. W. Baumgarte, Phys. Rev. D **97,** 084059 (2018).

[30] M. Shibata and T. Nakamura, Phys. Rev. D **52,** 5428 (1995).

[31] T. W. Baumgarte and S. L. Shapiro, Phys. Rev. D **59,** 024007 (1999).

[32] https://einsteintoolkit.org/.

[33] F. Löffler, J. Faber, E. Bentivegna, T. Bode, P. Diener, R. Haas, I. Hinder, B. C. Mundim, C. D. Ott, E. Schnetter, G. Allen, M. Campanelli, and P. Laguna, Classical Quantum Gravity **29,** 115001 (2012).

[34] V. Mewes, Y. Zlochower, M. Campanelli, T. W. Baumgarte, Z. B. Etienne, F. G. Lopez Armengol, and F. Cipolletta, Phys. Rev. D **101,** 104007 (2020).

[35] P. J. Montero, T. W. Baumgarte, and E. Müller, Phys. Rev. D **89,** 084043 (2014).

[36] D. Alic, C. Bona-Casas, C. Bona, L. Rezzolla, and C. Palenzuela, Phys. Rev. D **85,** 064040 (2012).

[37] D. Alic, W. Kastaun, and L. Rezzolla, Phys. Rev. D **88,** 064049 (2013).

[38] N. Sanchis-Gual, P. J. Montero, J. A. Font, E. Müller, and T. W. Baumgarte, Phys. Rev. D **89,** 104033 (2014).

[39] R. Courant, K. Friedrichs, and H. Lewy, Math. Ann. **100,** 32 (1928).

[40] C. Ronchi, R. Iacono, and P. Paolucci, J. Comput. Phys. **124,** 93 (1996).

[41] R. Gomez, L. Lehner, P. Papadopoulos, and J. Winicour, Classical Quantum Gravity **14,** 977 (1997).

[42] N. T. Bishop, R. Gómez, L. Lehner, M. Maharaj, and J. Winicour, Phys. Rev. D **56,** 6298 (1997).

[43] R. Gomez *et al.*, Phys. Rev. Lett. **80,** 3915 (1998).

[44] N. T. Bishop, R. Gomez, L. Lehner, B. Szilagyi, J. Winicour, and R. A. Isaacson, in *Black Holes, Gravitational Radiation, and the Universe: Essays in Honor of C.V. Vishveshwara*, edited by B. R. Iyer and B. Bhawal (Springer Science+Business Media, Dordrecht, 1999), p. 383.

[45] A. Kageyama and T. Sato, Geochem. Geophys. Geosyst. **5,** Q09005 (2004).

[46] J. Thornburg, Classical Quantum Gravity **21,** 3665 (2004).

[47] P. Diener, E. N. Dorband, E. Schnetter, and M. Tiglio, J. Sci. Comput. **32,** 109 (2007).

[48] L. Lehner, O. Reula, and M. Tiglio, Classical Quantum Gravity **22,** 5283 (2005).

[49] E. Schnetter, P. Diener, E. N. Dorband, and M. Tiglio, Classical Quantum Gravity **23,** S553 (2006).

[50] B. Zink, E. Schnetter, and M. Tiglio, Phys. Rev. D **77,** 103015 (2008).

[51] D. A. Calhoun, C. Helzel, and R. J. Leveque, SIAM Rev. **50,** 723 (2008).

[52] D. Pollney, C. Reisswig, E. Schnetter, N. Dorband, and P. Diener, Phys. Rev. D **83**, 044045 (2011).

[53] P. C. Fragile, C. C. Lindner, P. Anninos, and J. D. Salmonson, Astrophys. J. **691**, 482 (2009).

[54] A. Wongwathanarat, N. J. Hammer, and E. Müller, Astron. Astrophys. **514**, A48 (2010).

[55] T. Melson, H.-T. Janka, and A. Marek, Astrophys. J. Lett. **801**, L24 (2015).

[56] H. Shiokawa, R. M. Cheng, S. C. Noble, and J. H. Krolik, Astrophys. J. **861**, 15 (2018).

[57] S. W. Bruenn, J. M. Blondin, W. R. Hix, E. J. Lentz, O. E. B. Messer, A. Mezzacappa, E. Endeve, J. A. Harris, P. Marronetti, R. D. Budiardja, M. A. Chertkow, and C.-T. Lee, Astrophys. J. Suppl. Ser. **248**, 11 (2020).

[58] R. Sadourny, A. Arakawa, and Y. Mintz, Mon. Weather Rev. **96**, 351 (1968).

[59] Q. Du, Comput. Methods Appl. Mech. Eng. **192**, 3933 (2003).

[60] B. Müller, Mon. Not. R. Astron. Soc. **453**, 287 (2015).

[61] M. Liska, C. Hesp, A. Tchekhovskoy, A. Ingram, M. van der Klis, and S. Markoff, Mon. Not. R. Astron. Soc. **474**, L81 (2018).

[62] M. A. Skinner, J. C. Dolence, A. Burrows, D. Radice, and D. Vartanyan, Astrophys. J. Suppl. Ser. **241**, 7 (2019).

[63] B. Müller, T. M. Tauris, A. Heger, P. Banerjee, Y.-Z. Qian, J. Powell, C. Chan, D. W. Gay, and N. Langer, Mon. Not. R. Astron. Soc. **484**, 3307 (2019).

[64] K. Nakamura, T. Takiwaki, and K. Kotake, Publ. Astron. Soc. Jpn. **71**, 98 (2019).

[65] B. Zhang, K. A. Sorathia, J. G. Lyon, V. G. Merkin, and M. Wiltberger, J. Comput. Phys. **376**, 276 (2019).

[66] T. Dang, B. Zhang, J. Lei, W. Wang, A. Burns, H.-l. Liu, K. Pham, and K. A. Sorathia, Geosci. Model Dev. **14**, 859 (2021).

[67] R. Shapiro, Rev. Geophys. Space Phys. **8**, 359 (1970).

[68] P. R. Gent and M. A. Cane, J. Comput. Phys. **81**, 444 (1989).

[69] C. Jablonowski, Adaptive grids in weather and climate modeling, Ph.D. dissertation, University of Michigan, Ann Arbor, MI, 2004.

[70] O. Korobkin, E. B. Abdikamalov, E. Schnetter, N. Stergioulas, and B. Zink, Phys. Rev. D **83**, 043007 (2011).

[71] S. C. Noble, B. C. Mundim, H. Nakano, J. H. Krolik, M. Campanelli, Y. Zlochower, and N. Yunes, Astrophys. J. **755**, 51 (2012).

[72] J. F. Mahlmann, A. A. Philippov, V. Mewes, B. Ripperda, E. R. Most, and L. Sironi, Astrophys. J. Lett. **947**, L34 (2023).

[73] F. Banyuls, J. A. Font, J. M. Ibáñez, J. M. Martí, and J. A. Miralles, Astrophys. J. **476**, 221 (1997).

[74] L. Antón, O. Zanotti, J. A. Miralles, J. M. Martí, J. M. Ibáñez, J. A. Font, and J. A. Pons, Astrophys. J. **637**, 296 (2006).

[75] https://www.cactuscode.org.

[76] T. Goodale, G. Allen, G. Lanfermann, J. Massó, T. Radke, E. Seidel, and J. Shalf, in *High Performance Computing for Computational Science—VECPAR 2002* (Springer, Berlin, 2003).

[77] https://bitbucket.org/eschnett/carpet.

[78] E. Schnetter, S. H. Hawley, and I. Hawke, Classical Quantum Gravity **21**, 1465 (2004).

[79] J. G. Baker, M. Campanelli, and C. O. Lousto, Phys. Rev. D **65**, 044001 (2002).

[80] T. W. Baumgarte, P. J. Montero, I. Cordero-Carrion, and E. Muller, Phys. Rev. D **87**, 044026 (2013).

[81] T. W. Baumgarte, P. J. Montero, and E. Müller, Phys. Rev. D **91**, 064035 (2015).

[82] I. Ruchlin, Z. B. Etienne, and T. W. Baumgarte, Phys. Rev. D **97**, 064036 (2018).

[83] J. D. Brown, Phys. Rev. D **79**, 104029 (2009).

[84] C. Bona, J. Massó, E. Seidel, and J. Stela, Phys. Rev. Lett. **75**, 600 (1995).

[85] M. Alcubierre, B. Brügmann, P. Diener, M. Koppitz, D. Pollney, E. Seidel, and R. Takahashi, Phys. Rev. D **67**, 084023 (2003).

[86] R. J. Spiteri and S. J. Ruuth, SIAM J. Numer. Anal. **40**, 469 (2002).

[87] C.-W. Shu and S. Osher, J. Comput. Phys. **77**, 439 (1988).

[88] S. Gottlieb and C. W. Shu, Math. Comput. **67**, 73 (1998).

[89] D. S. Balsara, S. Garain, and C.-W. Shu, J. Comput. Phys. **326**, 780 (2016).

[90] M. Castro, B. Costa, and W. S. Don, J. Comput. Phys. **230**, 1766 (2011).

[91] A. Tchekhovskoy, J. C. McKinney, and R. Narayan, Mon. Not. R. Astron. Soc. **379**, 469 (2007).

[92] A. Suresh and H. T. Huynh, J. Comput. Phys. **136**, 83 (1997).

[93] D. S. Balsara and C.-W. Shu, J. Comput. Phys. **160**, 405 (2000).

[94] N. Fleischmann, S. Adami, and N. A. Adams, Comput. Fluids **189**, 94 (2019).

[95] L. Del Zanna, O. Zanotti, N. Bucciantini, and P. Londrillo, Astron. Astrophys. **473**, 11 (2007).

[96] Y. Chen, G. Tóth, and T. I. Gombosi, J. Comput. Phys. **305**, 604 (2016).

[97] P. Mösta, B. C. Mundim, J. A. Faber, R. Haas, S. C. Noble, T. Bode, F. Löffler, C. D. Ott, C. Reisswig, and E. Schnetter, Classical Quantum Gravity **31**, 015005 (2014).

[98] H.-O. Kreiss and J. Oliger, *Methods for the Approximate Solution of Time Dependent Problems*, GARP Publications Series – 10 (International Council of Scientific Unions, World Meteorological Organization, 1973).

[99] Z. B. Etienne, Y. T. Liu, V. Paschalidis, and S. L. Shapiro, Phys. Rev. D **85**, 064029 (2012).

[100] S. C. Noble, C. F. Gammie, J. C. McKinney, and L. Del Zanna, Astrophys. J. **641**, 626 (2006).

[101] P. Cerdá-Durán, J. A. Font, L. Antón, and E. Müller, Astron. Astrophys. **492**, 937 (2008).

[102] D. S. Balsara and D. Spicer, J. Comput. Phys. **148**, 133 (1999).

[103] S. C. Noble, J. H. Krolik, and J. F. Hawley, Astrophys. J. **692**, 411 (2009).

[104] S. M. Ressler, A. Tchekhovskoy, E. Quataert, and C. F. Gammie, Mon. Not. R. Astron. Soc. **467**, 3604 (2017).

[105] B. Einfeldt, SIAM J. Numer. Anal. **25**, 294 (1988).

[106] A. Harten, J. Comput. Phys. **49**, 357 (1983).

[107] O. Porth, H. Olivares, Y. Mizuno, Z. Younsi, L. Rezzolla, M. Moscibrodzka, H. Falcke, and M. Kramer, Comput. Astrophys. Cosmol. **4**, 1 (2017).

[108] M. Frigo and S. Johnson, Proc. IEEE **93**, 216 (2005).

[109] The $1 + \log$ [84] and "Γ-driver" [85] gauge conditions for the evolution of the lapse and shift we use in our evolution

can actually develop true shocks (see [141–144] for a description of the pathologies and gauge conditions that are shock-avoiding), but we haven't seen any evidence for the appearance of such gauge shocks and related problems with using the exponential filter for the spacetime fields in our simulations. The shock-avoiding slicing conditions of [141,144] were shown to be a viable alternative to the $1 + \log$ slicing condition [145], which means they could be used in conjunction with the exponential filter in situations that are prone to the development of gauge shocks.

[110] A. Jameson, W. Schmidt, and E. Turkel, in *Proceedings of the 14th Fluid and Plasma Dynamics Conference, Palo Alto, CA, USA* (1981), p. 1259.

[111] H.-J. Yo, T. W. Baumgarte, and S. L. Shapiro, Phys. Rev. D **66,** 084026 (2002).

[112] J. M. Bowen and J. W. York, Jr., Phys. Rev. D **21,** 2047 (1980).

[113] M. Ansorg, B. Brügmann, and W. Tichy, Phys. Rev. D **70,** 064011 (2004).

[114] J. Thornburg, Classical Quantum Gravity **21,** 743 (2004).

[115] E. Schnetter, F. Herrmann, and D. Pollney, Phys. Rev. D **71,** 044033 (2005).

[116] J. Thornburg, Living Rev. Relativity **10,** 3 (2007).

[117] O. Dreyer, B. Krishnan, D. Shoemaker, and E. Schnetter, Phys. Rev. D **67,** 024018 (2003).

[118] E. Schnetter, B. Krishnan, and F. Beyer, Phys. Rev. D **74,** 024028 (2006).

[119] M. Campanelli, C. O. Lousto, Y. Zlochower, B. Krishnan, and D. Merritt, Phys. Rev. D **75,** 064030 (2007).

[120] A. Komar, Phys. Rev. **113,** 934 (1959).

[121] V. Mewes, J. A. Font, and P. J. Montero, Phys. Rev. D **91,** 124043 (2015).

[122] B. C. Mundim, B. J. Kelly, Y. Zlochower, H. Nakano, and M. Campanelli, Classical Quantum Gravity **28,** 134003 (2011).

[123] G. Reifenberger and W. Tichy, Phys. Rev. D **86,** 064003 (2012).

[124] H. Okawa, H. Witek, and V. Cardoso, Phys. Rev. D **89,** 104032 (2014).

[125] P. Cerdá-Durán, J. A. Font, L. Antón, and E. Müller, Astron. Astrophys. **492,** 937 (2008).

[126] K. Beckwith and J. M. Stone, Astrophys. J. Suppl. Ser. **193,** 6 (2011).

[127] N. Stergioulas, T. A. Apostolatos, and J. A. Font, Mon. Not. R. Astron. Soc. **352,** 1089 (2004).

[128] N. Stergioulas and J. L. Friedman, Astrophys. J. **444,** 306 (1995).

[129] L. Franci, R. De Pietri, K. Dionysopoulou, and L. Rezzolla, Phys. Rev. D **88,** 104028 (2013).

[130] M. Shibata, T. W. Baumgarte, and S. L. Shapiro, Astrophys. J. **542,** 453 (2000).

[131] N. Andersson, Classical Quantum Gravity **20,** R105 (2003).

[132] V. Paschalidis and N. Stergioulas, Living Rev. Relativity **20,** 7 (2017).

[133] E. Velikhov, Sov. Phys. JETP **36,** 995 (1959).

[134] S. Chandrasekhar, Proc. Natl. Acad. Sci. U.S.A. **46,** 253 (1960).

[135] S. A. Balbus and J. F. Hawley, Astrophys. J. **376,** 214 (1991).

[136] S. A. Balbus and J. F. Hawley, Rev. Mod. Phys. **70,** 1 (1998).

[137] L. Baiotti, R. de Pietri, G. M. Manca, and L. Rezzolla, Phys. Rev. D **75,** 044023 (2007).

[138] M. D. Duez, Y. T. Liu, S. L. Shapiro, M. Shibata, and B. C. Stephens, Phys. Rev. D **73,** 104015 (2006).

[139] J. D. Hunter, Comput. Sci. Eng. **9,** 90 (2007).

[140] W. Kastaun, PYCactus: Post-processing tools for Cactus computational toolkit simulation data, Astrophysics Source Code Library, record ascl:2107.017 (2021), ascl:2107.017.

[141] M. Alcubierre, Phys. Rev. D **55,** 5981 (1997).

[142] M. Alcubierre and J. Massó, Phys. Rev. D **57,** R4511 (1998).

[143] M. Alcubierre, Classical Quantum Gravity **22,** 4071 (2005).

[144] M. Alcubierre, Classical Quantum Gravity **20,** 607 (2003).

[145] T. W. Baumgarte and D. Hilditch, Phys. Rev. D **106,** 044014 (2022).